Time-delayed luminescence spectral measurement

The time-delayed luminescence spectra of 4AMF-DOTA(Nd) (10 μmol/L) were measured in 10 mmol/L Tris–HCl buffer, pH 8.0, at 25°C, following excitation at 488 nm. A delay time of 7 μs and a gate time of 100 μs were used.

UV-visible absorption spectral measurement

The absorption spectral changes of 4AMF-DOTA(Nd) (10 μmol/L) in 10 mmol/L Tris–HCl buffer, pH 8.0, at 25°C were determined.

Luminescence lifetime measurements

The luminescence lifetime of 4AMF-DOTA(Nd) (10 μmol/L) in 10 mmol/L Tris–HCl buffer, pH 8.0, at 25°C was determined. Data were collected at 1 μs resolution and fitted to a single-exponential curve using the equation shown below, where I_0 and I are the luminescence intensities at time $t = 0$ and time t, respectively, and τ is the luminescence emission lifetime. Lifetime was obtained by monitoring emission intensity at 870 nm ($\lambda_{ex} = 488$ nm):

$$I = I_0 \exp(-t/\tau)$$

Synthesis

4-(Chloromethylamido)fluorescein (4AMF-Cl). 4-Aminofluorescein (1.0 g, 3.0 mmol) was dissolved in acetone (20 mL). To the solution was added $ClCH_2COCl$ (372 mg, 3.3 mmol) in acetone solution (10 mL). A yellow powder was formed instantly. The mixture was then stirred for 5 h at room temperature. The mixture was concentrated by evaporation and the resulting residue was redissolved in MeOH. The solution was poured into Et_2O (200 mL), and the resulting residue was washed with Et_2O by decantation three times. The powder was dried under vacuum to obtain 4AMF-Cl (852 mg, 1.9 mmol, 61%) as a yellow powder. MS (ESI, pos.), m/z found 425 ($[M+H]^+$), calcd. 425 ^{1}H-NMR (400 MHz, CD_3OD) δ 8.60 (1H, d, $J = 2.2$ Hz), 8.16 (1H, dd, $J = 2.2$, 8.3 Hz), 7.48 (2H, d, $J = 9.0$ Hz), 7.44 (1H, d, $J = 8.3$ Hz), 7.29 (2H, d, $J = 2.2$ Hz), 7.14 (2H, dd, $J = 2.2$, 9.0 Hz), 4.29 (2H, s).

1-(4-Amidomethyl-fluorescein)-1,4,7,10-tetraazacyclododecane (4AMF-cyclen). A dry DMF suspension (10 mL) of 1,4,7,10-tetraazacyclododecane tetrahydrochloride (cyclen 4HCl) (318 mg, 1.0 mmol), K_2CO_3 (1.4 g, 10.1 mmol) and KI (1.7 g, 10.1 mmol) was stirred for 5 min at 80°C under anaerobic conditions. To the suspension was then slowly added 4AMF-Cl (424 mg, 1.0 mmol) in dry DMF solution (10 mL). After stirring for 9 h at 80°C, the suspension was filtered and the obtained residue was washed with MeCN. The residue was added to MeOH (20 mL). After stirring for 30 min, the reddish suspension was filtered and the obtained residue was washed with MeOH. The filtrate was concentrated by evaporation and the resulting residue was redissolved in a minimum amount of MeOH. The solution was poured into Et_2O (200 mL), and the resulting residue was washed with Et_2O by decantation three times. The powder was dried under vacuum to obtain 4AMF-cyclen (336 mg, 0.6 mmol, 60%) as a red powder. MS (ESI, pos.) m/z found 560 ($[M+H]^+$), calcd. 560. ^{1}H-NMR (400 MHz, DMSO-d_6) δ 8.38 (1H, s), 7.91 (1H, d, $J = 7.3$ Hz), 6.62 (3H, m), 6.52 (2H, s), 6.44 (2H, dd, $J = 1.9$, 8.7 Hz), 3.17 (2H, s), 2.66 (16H, br).

1-(4-Amidomethyl-fluorescein)-1,4,7,10-tetraazacyclododecane-4,7,10-triacetic acid (4AMF-DOTA). To MeOH solution containing 4AMF-cyclen (559.6 mg, 1.0 mmol) and Et_3N (1.4 mL, 10 mmol) was added $BrCH_2COOH$ (556 mg, 4.0 mmol) in MeOH (20 mL) solution at room temperature. The solution was then warmed to 60°C and stirred for 12 h. The mixture was evaporated to remove the solvent. The yellow residue was added to MeOH (20 mL). The suspension was centrifuged (1500 × g, 10 min) and the supernatant was removed. This procedure was repeated five times. The resulting powder was dried under vacuum to obtain 4AMF-DOTA (550.3 mg, 0.8 mmol, 75%) as a yellow powder. MS (ESI, neg.) m/z found 732 ($[M-H]^-$), calcd. 732.

^{1}H-NMR (400 MHz, DMSO-d_6) δ 8.24 (1H, s), 7.68 (1H, s), 6.50–6.70 (7H, m), 4.15 (6H, br), 3.16 (18H, m).

4AMF-DOTA(Nd). To 0.01 mol/L TEAAc buffer, pH 6.5, solution (2 mL) containing 4AMF-DOTA (7.3 mg, 10 μmol) was added $NdCl_3$ $6H_2O$ (4.3 mg, 15 μmol) in 0.01 mol/L TEAAc buffer, pH 6.5, solution (2 mL). After stirring for 1 h at room temperature, the resulting suspension was filtered. The filtrate was introduced into a preconditioned solid phase extraction column (Waters, stationary phase C_{18}) and the buffer and excess lanthanide ion were washed away with distilled water. The chelate was eluted using a 1:4 methanol:water mixture. The solvent was evaporated, and the residue was dried under vacuum to obtain 4AMF-DOTA(Nd) (5.4 mg, 6.2 μmol, 62%) as a yellow powder. MS(ESI, neg.) m/z found 882 ($[M-H]^-$), calcd. 882.

RESULTS AND DISCUSSION

Synthesis of 4AMF-DOTA(Nd)

4AMF-DOTA was synthesized from 4-aminofluorescein in three steps, as shown in Scheme 1. 4AMF-DOTA(Nd)

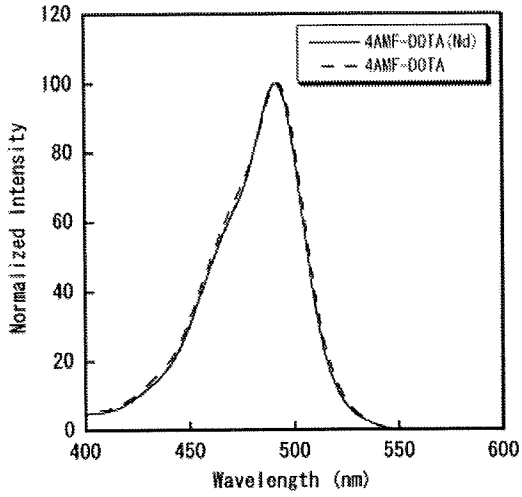

Figure 1. UV-vis absorption spectra of 4AMF-DOTA (dotted line) and 4AMF-DOTA(Nd) (solid line) in 10 mmol/L Tris–HCl buffer, pH 8.0.

was easily synthesized by stirring 4AMF-DOTA and $NdCl_3$ in TEAAc buffer, pH 6.5. Other lanthanide complexes, 4AMF-DOTA(Ln) (Ln = Eu, Tb and Yb), were prepared by the same method as for preparing 4AMF-DOTA(Nd), using $EuCl_3$, $TbCl_3$ and $YbCl_3$.

Spectroscopic characterizations of aqueous solution of 4AMF-DOTA(Nd)

UV-vis spectra of aqueous solutions of 4AMF-DOTA(Nd) and 4AMF-DOTA are shown in Fig. 1. These spectra showed the same features, suggesting that the chelation of DOTA to the Nd ion has no effect on the energy level of the fluorescein moiety.

With IR measurement, absorption of the carbonyl C=O stretching was observed at 1749 cm^{-1} for 4AMF-DOTA and 1724 cm^{-1} for 4AMF-DOTA(Nd), and absorption of the amide N–H bending was found at 1609 cm^{-1} for 4AMF-DOTA and 1587 cm^{-1} for 4AMF-DOTA(Nd) (data not shown). These shifts suggest that the three carbonyl groups and one amide group of the DOTA moiety participated in chelating the Nd ion.

The emission spectra of aqueous solutions of 4AMF-DOTA(Nd) and 4AMF-DOTA are shown in Fig. 2A. Although the long-wavelength tail of fluorescein fluorescence was observed in both compounds, two sharp peaks were detected at 870–900 nm in the spectrum of 4AMF-DOTA(Nd) compared with that of 4AMF-DOTA (Fig. 2A, $\lambda_{ex} = 488$ nm). These can be assigned to typical Nd $^4F_{3/2}$ to $^4I_{9/2}$ transition. This excitation wavelength is only slightly injurious to living cells. On the other hand, no fluorescent peak was detected for $NdCl_3$ and Nd-DOTA under the same conditions.

The excitation spectra of aqueous solutions of 4AMF-DOTA(Nd) and 4AMF-DOTA showed much the same features (Fig. 2B, $\lambda_{em} = 870$ nm for 4AMF-DOTA(Nd) and 515 nm for 4AMF-DOTA), thus supporting that the 870–900 nm luminescence shown in 4AMF-DOTA(Nd) is derived from the transfer of energy from an excited fluorescein moiety.

These results indicate that 4AMF-DOTA(Nd) can emit NIR fluorescence through its excitation by visible light as expected, but the fluorescence intensity is lower than that from fluorescein. This might occur partly because of the very low triplet yield of excited fluorescein. A simple model for the description of the sensitization process is shown in Fig. 3 (17). Energy transfer from fluorescein to the Nd ion occurs in the triplet state of fluorescein. Moreover, singlet energy transfer has been

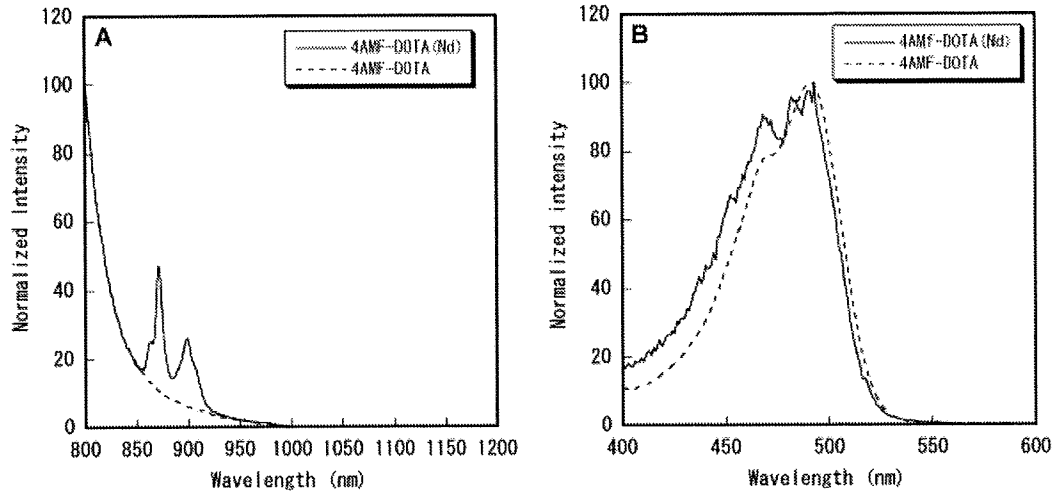

Figure 2. Spectroscopy of 4AMF-DOTA (dotted line) and 4AMF-DOTA(Nd) (solid line) in 10 mmol/L Tris–HCl buffer, pH 8.0. (A) Emission spectra ($\lambda_{ex} = 488$ nm). (B) Excitation spectra ($\lambda_{ex} = 870$ nm for 4AMF-DOTA(Nd) and 515 nm for 4AMF-DOTA).

Luminescence 2007; 22: 455–461
DOI: 10.1002/bio

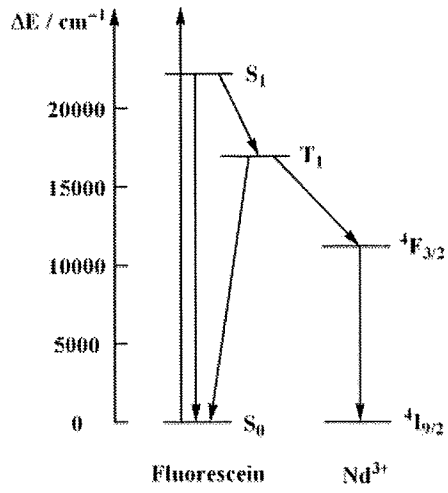

Figure 3. Simple photophysical scheme describing a possible pathway for sensitization of Nd luminescence in 4AMF-DOTA(Nd).

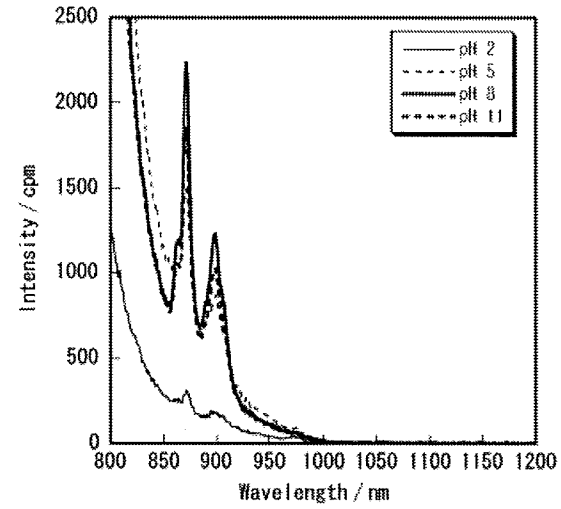

Figure 4. pH effect on the emission spectra of 4AMF-DOTA(Nd) in 10 mmol/L Britton–Robinson buffer.

shown not to contribute significantly to the sensitization process (18).

The energy transfer from the antenna to lanthanide ion has been studied previously (19–21), which has suggested several mechanisms, such as Förster energy transfer (19), Dexter exchange (20) and sequential electronic interaction (21), although none of them has been fully elucidated yet and the mechanism involved in 4AMF-DOTA(Nd) is also unclear. Refining the energy level of fluorescein through derivative syntheses (15) or the use of other chromophores (22, 23) suitable for the Nd ion can be an effective solution.

On the other hand, 4AMF-DOTA(Yb) showed a small peak at approximately 1000 nm due to typical ytterbium $^2F_{5/2}$ to $^2F_{7/2}$ transition, whereas emission peaks of 4AMF-DOTA(Eu) and 4AMF-DOTA(Tb) were not observed, owing to their high excitation levels.

Effects of pH and solvent on the fluorescence of 4AMF-DOTA(Nd)

The effect of pH on the fluorescence of 4AMF-DOTA(Nd) was examined (Fig. 4). The fluorescent intensity of 4AMF-DOTA(Nd) was weak at pH 2, increased with pH and peaked at pH 8. In the pH range 2–11, no degradation product was detected by electrospray mass spectral (ESI–MS) analysis, suggesting the high stability of 4AMF-DOTA(Nd).

It is well known that the fluorescence intensity emitted by fluorescein varies depending on the pH of solvents. The dianionic form of fluorescein in neutral and basic solutions is the most effective to emit fluorescence. In other words, in acidic solution, transition to the ground state of excited fluorescein is carried out without a fluorescent process (24). Therefore, the results shown in Fig. 4 should be regarded as a reflection of the characteristics of fluorescein, supporting the occurrence of energy transfer from fluorescein, the antenna moiety, to the Nd ion.

4AMF-DOTA(Nd) could easily dissolve in many polar organic solvents (e.g. MeOH, EtOH and DMSO). Figure 5 shows the emission spectra (Fig. 5A) and the excitation spectra (Fig. 5B) of 4AMF-DOTA(Nd) in 10 mmol/L Tris–HCl buffer, pH 8.0, and organic solvents such as MeOH, EtOH and DMSO. The λ_{max} of the excitation wavelength against 870 nm emission was 488 nm in aqueous buffer and 498, 504 and 523 nm in MeOH, EtOH and DMSO, respectively (Fig. 5B). On the other hand, the emission spectra showed the same features in the four tested solvents except for intensity at 870 nm and 890 nm (Fig. 5A). This difference in the wavelength shift between excitation and emission spectra may emphasize the orientation of fluorescence, i.e. the results can be considered as follows. In excitation spectra, changes of the λ_{max} in organic solvents are caused by the effect on the energy levels of fluorescein by the solvents, and in the emission spectra the constant wavelength in the four solvents is due to the characteristic of lanthanide ions, that 5s and 5d orbitals are located outside the 4f orbital responsible for fluorescence and protect it from environmental changes. In other words, these data further support that fluorescence around 870–900 nm derives from the Nd ion through energy transfer from the antenna moiety. The emission intensity of 4AMF-DOTA(Nd) shown more strongly in organic solvents than in buffer is probably because H_2O acts as a quencher against excited 4AMF-DOTA(Nd) in some processes.

Long-lived luminescence measurement

Time-resolved fluorescent (TRF) measurement can extract long-lived luminescence. Figure 6 shows the

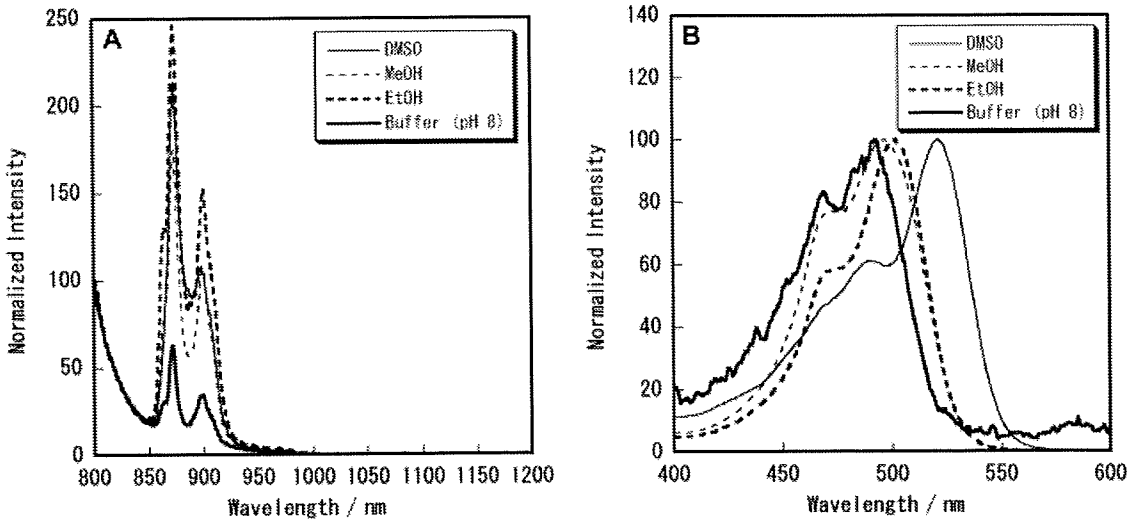

Figure 5. Solvent effect on (A) emission spectra and (B) excitation spectra of 4AMF-DOTA(Nd) in 10 mmol/L Tris–HCl buffer, pH 8.0, MeOH, EtOH and DMSO; each organic solvent contained 0.1% v/v Et_3N.

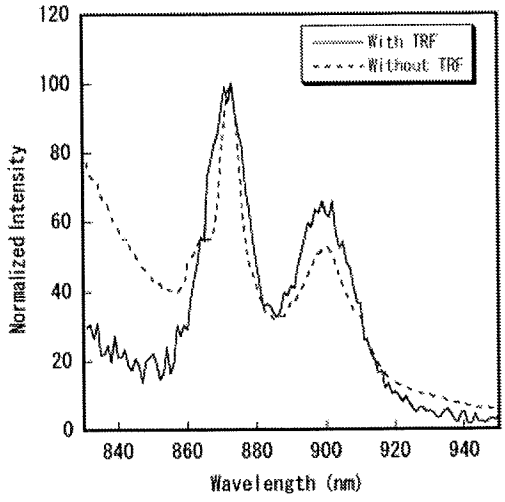

Figure 6. Emission spectra of 4AMF-DOTA(Nd) in 10 mmol/L Tris–HCl buffer, pH 8.0, with (solid line) and without (dotted line) time-resolved measurement.

emission spectra of 4AMF-DOTA(Nd) detected with (solid line) and without (dotted line) TRF measurement. The luminescence of fluorescein and the Nd ion was observed without TRF measurement, as also shown in Fig. 2A, whereas the luminescence of fluorescein disappeared in the detection of emission spectrum with TRF measurement, resulting in the extraction of only Nd luminescence. Furthermore, we calculated the lifetime of Nd ion luminescence using the equation described in the Experimental section. A lifetime of 2.3 μs was consequently obtained as reasonable for a Nd complex, as reported previously (10, 17). In view of the ns-order lifetime of fluorescein [~4 ns (25)], 4AMF-DOTA(Nd) can be considered a potential NIR fluorescent probe able to be detected and imaged separately from fluorescein, scattered or reflected excitation light and other organic fluorophores by the TRF technique.

CONCLUSION

The results obtained in this study indicate that 4AMF-DOTA(Nd) has the potential for *in vivo* fluorescence imaging, with several favourable properties, such as near-infrared luminescence, visible light excitation, long lifetime and large Stoke's shift.

Acknowledgement

This work was partly supported by the Twenty-first Century Center of Excellence Programme 'Knowledge Information Infrastructure for Genome Science'.

REFERENCES

1. Fu G, Yang HY, Wang C, Zhang F, You ZD, Wang GY, He C, Chen YZ, Xu ZZ. Detection of constitutive heterodimerization of the integrin Mac-1 subunits by fluorescence resonance energy transfer in living cells.*Biochem. Biophys. Res. Commun.*2006; **346**: 986.
2. Wandelt B, Cywinski P, Darling GD, Stranix BR. Single cell measurement of micro-viscosity by ratio imaging of fluorescence of styrylpyridinium probe. *Biosens. Bioelectron.* 2005; **20**: 1728.
3. Mizukami S, Kikuchi K, Higuchi T, Urano Y, Mashima T, Tsuruo T, Nagano T. Imaging of caspase-3 activation in HeLa cells stimulated with etoposide using a novel fluorescent probe. *FEBS Lett.* 1999; **453**: 356.
4. Konig K. Multiphoton microscopy in life sciences*J. Microsc.* 2000; **200**: 83.
5. Hansch A, Frey O, Sauner D, Hilger I, Haas M, Malich A, Brauer R, Kaiser WA. *In vivo* imaging of experimental arthritis with near-infrared fluorescence. *Arthrit. Rheum.* 2004; **50**: 961.

6. Chen X, Conti PS, Moats RA. *In vivo* near-infrared fluorescence imaging of integrin $\alpha v\beta 3$ in brain tumor xenografts. *Cancer Res.* 2004; **64**: 8009.
7. Wunder A, Tung CH, Muller-Ladner U, Weissleder R, Mahmood U. *In vivo* imaging of protease activity in arthritis: a novel approach for monitoring treatment response. *Arthrit. Rheum.* 2004; **50**: 2459.
8. Faulkner S, Carrie MC, Pope SJ, Squire J, Beeby A, Sammes PG. Pyrene-sensitized near-IR luminescence from ytterbium and neodymium complexes. *Dalton Trans.* 2004; 1405.
9. Beer PD, Szemes F, Passaniti P, Maestri M. Luminescent ruthenium(II) bipyridine-calix[4]arene complexes as receptors for lanthanide cations. *Inorg. Chem.* 2004; **43**: 3965.
10. Hasegawa Y, Ohkubo T, Sogabe K, Kawamura Y, Wada Y, Nakashima N, Yanagida S. Luminescence of novel neodymium sulfonylaminate complexes in organic media. *Angew. Chem. Int. Ed. Engl.* 2000; **39**: 357.
11. Becker CF, Clayton D, Shapovalov G, Lester HA, Kochendoerfer GG. On-resin assembly of a linkerless lanthanide(III)-based luminescence label and its application to the total synthesis of site-specifically labeled mechanosensitive channels. *Bioconjug. Chem.* 2004; **15**: 1118.
12. Wu SL, Horrocks WD. Direct determination of stability constants of lanthanide ion chelates by laser-excited europium(III) luminescence spectroscopy: application to cyclic and acyclic aminocarboxylate complexes. *J. Chem. Soc. Dalton* 1997; 1497.
13. Quici S, Marzanni G, Forni A, Accorsi G, Barigelletti F. New lanthanide complexes for sensitized visible and near-IR light emission: synthesis, ^{1}H-NMR, and X-ray structural investigation and photophysical properties. *Inorg. Chem.* 2004; **43**: 1294.
14. Werts MHV, Hofstraat JW, Geurts FAJ, Verhoeven JW. Fluorescein and eosin as sensitizing chromophores in near-infrared luminescent ytterbium(III), neodymium(III) and erbium(III) chelates. *Chem. Phys. Lett.* 1997; **276**: 196.
15. Nolan EM, Burdette SC, Harvey JH, Hilderbrand SA, Lippard SJ. Synthesis and characterization of zinc sensors based on a monosubstituted fluorescein platform. *Inorg. Chem.* 2004; **43**: 2624.
16. Brown L, Halling PJ, Johnston GA, Suckling CJ, Valivety RH. The synthesis of some water-insoluble dyes for the measurement of pH in water-immiscible solvents. *J. Chem. Soc. Perk. Trans.* **1**: 1990; 3349.
17. Bassett AP, Magennis SW, Glover PB, Lewis DJ, Spencer N, Parsons S, Williams RM, De Cola L, Pikramenou Z. Highly luminescent, triple- and quadruple-stranded, dinuclear Eu, Nd, and Sm(III) lanthanide complexes based on bis-diketonate ligands. *J. Am. Chem. Soc.* 2004; **126**: 9413.
18. Crosby GA, Alire RM, Whan RE. Intramolecular energy transfer in rare earth chelates – role of triplet state*J. Chem. Phys.* 1961; **34**: 743.
19. Clarkson IM, Beeby A, Bruce JI, Govenlock LJ, Lowe MP, Mathieu CE, Parker D, Senanayake K. Experimental assessment of the efficacy of sensitized emission in water from a europium ion, following intramolecular excitation by a phenanthridinyl group*N. J. Chem.* 2000; **24**: 377.
20. Barigelletti F, Flamigni L, Balzani V, Collin JP, Sauvage JP, Sour A, Constable EC, Thompson AMWC. Intramolecular energy transfer through phenyl bridges in rod-like dinuclear Ru(II)/Os(II) terpyridine-type complexes. *Coord. Chem. Rev.* 1994; **132**: 209.
21. Faulkner S, Burton-Pye BP, Khan T, Martin LR, Wray SD, Skabara PJ. Interaction between tetrathiafulvalene carboxylic acid and ytterbium D03A: solution state self-assembly of a ternary complex which is luminescent in the near IR. *Chem. Commun.* 2002; 1668.
22. Gunnlaugsson T, MacDonaill DA, Parker D. Lanthanide macrocyclic quinolyl conjugates as luminescent molecular-level devices. *J. Am. Chem. Soc.* 2001; **123**: 12866.
23. Quici S, Marzanni G, Cavazzini M, Anelli PL, Botta M, Gianolio E, Accorsi G, Armaroli N, Barigelletti F. Highly luminescent Eu^{3+} and Tb^{3+} macrocyclic complexes bearing an appended phenanthroline chromophore. *Inorg. Chem.* 2002; **41**: 2777.
24. Urano Y, Kamiya M, Kanda K, Ueno T, Hirose K, Nagano T. Evolution of fluorescein as a platform for finely tunable fluorescence probes. *J. Am. Chem. Soc.* 2005; **127**: 4888.
25. Thevenin BJM, Periasamy N, Shohet SB, Verkman AS. Segmental dynamics of the cytoplasmic domain of erythrocyte band 3 determined by time-resolved fluorescence anisotropy – sensitivity to pH and ligand-binding. *Proc. Natl Acad. Sci. USA* 1994; **91**: 1741.

Prominent Lectin-Like Oxidized Low Density Lipoprotein (LDL) Receptor-1 (LOX-1) Expression in Atherosclerotic Lesions Is Associated with Tissue Factor Expression and Apoptosis in Hypercholesterolemic Rabbits

Yuji KUGE,*[a,b] Noriaki KUME,[c] Seigo ISHINO,[a] Nozomi TAKAI,[a] Yuki OGAWA,[a] Takahiro MUKAI,[d] Manabu MINAMI,[c] Masashi SHIOMI,[c] and Hideo SAJI[a]

[a] *Department of Patho-functional Bioanalysis, Graduate School of Pharmaceutical Sciences, Kyoto University; Yoshida Shimoadachi-cho, Sakyo-ku, Kyoto 606–8501, Japan:* [b] *Department of Tracer Kinetics & Bioanalysis, Graduate School of Medicine, Hokkaido University; Kita 15 Nishi 7, Kita-ku, Sapporo 060–8638, Japan:* [c] *Department of Cardiovascular Medicine, Graduate School of Medicine, Kyoto University; Konoe-cho, Yoshida, Sakyo-ku, Kyoto 606–8501, Japan:* [d] *Department of Biomolecular Recognition Chemistry, Graduate School of Pharmaceutical Sciences, Kyushu University; 3–1–1 Maidashi, Higashi-ku, Fukuoka 812–8582, Japan: and* [e] *Institute for Experimental Animals, Kobe University School of Medicine; 7–5–1 Kusunoki-cho, Chuo-ku, Kobe 650–0017, Japan.*

Received April 8, 2008; accepted May 13, 2008; published online May 15, 2008

Background: Despite increasing *in vitro* evidence that lectin-like oxidized low density lipoprotein (LDL) receptor-1 (LOX-1), a cell-surface receptor for oxidized LDL, is implicated in the atherogenesis and thrombus formation, its *in vivo* participation to the atherosclerotic plaque destabilization, rupture and thrombus formation remains unclear. Here, we compared the *in vivo* expression of LOX-1, with tissue factor (TF) expression and cell apoptosis, in atherosclerotic lesions of myocardial infarction-prone Watanabe heritable hyperlipidemic (WHHLMI) rabbits. Methods and Results: We prepared sixty series of cross sections in the aortic arch and the thoracic aorta from four WHHLMI rabbits. LOX-1 and TF expression, as well as apoptotic events were determined by immunohistochemical staining and TUNEL methods, respectively. LOX-1 expression was mainly observed in the macrophage-rich lipid areas of vulnerable plaque-like atheromatous lesions where TF expression and apoptotic events were prominent. LOX-1 expression was positively correlated with TF expression (r=0.53, p<0.0001), apoptotic events (r=0.52, p<0.0001) and morphological vulnerability (r=0.63, p<0.0001). Conclusions: LOX-1 expression appears to be closely associated with TF expression, apoptotic events and the morphological vulnerability, suggesting the *in vivo* involvement of LOX-1 in the destabilization and rupture of atherosclerotic lesions and the subsequent thrombus formation. The present findings in hypercholesterolemic rabbits should help advance our understanding of the pathophysiology of atherosclerosis.

Key words lectin-like oxidized low density lipoprotein receptor-1; tissue factor; apoptosis; atherosclerosis

Rupture or erosion of vulnerable atherosclerotic plaques and the subsequent formation of occlusive thrombi are currently recognized as the primary causes of acute coronary syndrome and stroke.[1] Vulnerability of atherosclerotic plaques, rather than severity of luminal stenosis, has been suggested to be the most important determinant for the onset of acute coronary syndrome.[2] Accordingly, it is of great importance to determine causative factors in the destabilization of atherosclerotic plaques and in the thrombus formation, which should help develop new therapeutic and diagnostic (imaging) agents of atherosclerosis, leading to the establishment of novel therapeutic strategies for preventing acute coronary syndromes and stroke.

To date, enhanced proinflammatory responses and the expression of matrix metalloproteinases (MMPs) have been suggested to play important roles in the destabilization of atherosclerotic plaques. Apoptosis and prothrombotic factors in atherosclerotic plaques have also been reported to be crucial factors for the plaque vulnerability and thrombus formation.[3] Apoptosis of foam cells and macrophages contributes to the formation of an acellular (cell-poor) lipid core,[4] and the apoptosis of smooth muscle cells further weaken the fibrous cap by decreasing the synthesis of extracellular matrix proteins.[5] Tissue factor (TF), a cofactor for plasma coagulation factor VIIa, which is localized in vascular cells and the lipid core within the atherosclerotic lesions, is an initiator of the coagulation cascade leading to thrombus formation after the plaque rupture *in vivo*.[3]

Lectin-like oxidized low density lipoprotein (LDL) receptor-1 (LOX-1), a type II membrane glycoprotein belonging to the C-type lectin family, acts as a cell-surface receptor for oxidized LDL (Ox-LDL) and mediates several biological effects of Ox-LDL.[6] Recent studies with cultured cells suggest that LOX-1 may play several important roles in destabilization of atherosclerotic plaques, inducing expression of adhesion molecules and chemokines for monocytes,[7] transformation of macrophages into foam cells,[8,9] apoptosis of smooth muscle cells[10,11] and the degradation of extracellular matrix proteins by induction of matrix metalloproteinases.[12] Several studies with cultured cells also showed that Ox-LDL, through LOX-1, also triggers the CD40/CD40L signaling pathway,[13,14] which then induce TF expression.[15] These biological effects mediated by Ox-LDL-LOX-1 interactions may enlarge the lipid core, weaken the fibromuscular cap, and induce proinflammatory responses, resulting in destabilization of the atherosclerotic plaques and thrombus formation.

The actual contribution of LOX-1 to the plaque vulnerability and thrombus formation *in vivo*, however, remains unclear. In this context, we recently demonstrated that LOX-1 expression is related to MMP-9 expression and morphological plaque vulnerability using a rabbit model of spontaneous atherosclerosis,[16] myocardial infarction-prone Watanabe her-

* To whom correspondence should be addressed. e-mail: kuge@med.hokudai.ac.jp

itable hyperlipidemic (WHHLMI) rabbits (previous strain: Watanabe heritable hyperlipidemic (WHHL) rabbits). The use of WHHLMI rabbits could be effective for investigating causative factors in the destabilization of atherosclerotic plaques, as the histological characteristics of their atherosclerotic lesions have been reported to be similar to those of humans.[17,18] Thus, in the present study, we compared LOX-1 expression with TF expression and apoptosis in atherosclerotic lesions of WHHLMI rabbits, in order to further characterize the roles of LOX-1 to the plaque vulnerability and thrombus formation *in vivo*.

MATERIALS AND METHODS

Animals Four WHHLMI rabbits (female, 12.6±0.8 months old: 3.7±0.3 kg body weight) bred at Kobe University were used in the present study. The rabbits were fed standard rabbit chow (type CR-3; Clea Japan Inc., Tokyo, Japan: 120 g/d) and were given water *ad libitum*. All experimental procedures were approved by the Kyoto University Animal Care Committee.

Preparation of Histological Sections Rabbits were sacrificed with an overdose of sodium pentobarbital (Nembutal, intravenously, Dainippon Sumitomo Pharma, Osaka, Japan). The aortic arch and thoracic aorta were cut into 6 and 9 segments, respectively. Each segment was immediately fixed in a solution containing L-(+)-lysine hydrochloride (75 mmol/l) and 4% paraformaldehyde in phosphate buffer (37.5 mmol/l; pH 7.4), and embedded in paraffin. Consecutive 5-μm thick slices were prepared at the center of each segment.

Histological Analysis Serial sections were subjected to immunostaininig for LOX-1, TF and cell type marker antigens, as well as HE and Azan–Mallory staining. A monoclonal antibody for rabbit LOX-1 (mouse IgG) was established by a standard hybridoma technique.[16] Its specificity was confirmed in CHO cells stably expressing rabbit LOX-1 (data not shown). A monoclonal antibody for rabbit TF (mouse IgG) was obtained from American Diagnostica (Stanford, CA, U.S.A.). Monoclonal antibodies for a rabbit macrophage-specific antigen (RAM-11, mouse IgG) and smooth muscle actin (1A4, mouse IgG) were obtained from Dako Corp., Santa Barbara, CA, U.S.A. Immunohistochemical staining was carried out using a Dako Envision+kit (Dako) with hematoxylin counterstaining. Immunostaining with subclass-matched irrelevant IgG served as a negative control. Apoptotic nuclei were determined by terminal deoxyribonucleotide transferase (TdT)-mediated nick-end labeling (TUNEL) using a commercially available kit (*in situ* apoptosis detection kit, TACS, Trevigen, Gaithersburg, MD, U.S.A.).[19] Specimens stained without TdT enzyme served as negative controls. Counterstaining with hematoxylin was also performed. Tissue fixation, paraffin embedding, and LOX-1 and TF staining procedure were performed in the same condition, respectively.

Classification of Atherosclerotic Lesions The atherosclerotic lesions in WHHLMI rabbits were divided into 4 categories using a classification scheme based on the recommendations of the American Heart Association (AHA)[20,21] by HE and Azan–Mallory staining, as previously described[19]: (1) neointimal lesion (Type I—III), (2) atheromatous lesion (Type IV), (3) fibroatheromatous lesion (Type Va, Vb), (4) collagen-rich lesion (Type Vc), as shown in Fig. 1. Neointimal lesions were defined as having adaptive thickening of the intima consisting mainly of smooth muscle cells and few macrophages. Atheromatous lesions consisted of macrophages (foam cells) rich and lipid-rich areas covered with thin fibrous connective tissue, and were considered to be similar to vulnerable lesions in human atherosclerotic plaques. Fibroatheromatous lesions were composed of several macrophages (foam cells) and lipid-rich areas separated by thick layers of fibromuscular connective tissue, which were relatively stable to rupture.[22] Collagen-rich lesions contained predominant collagen components and smooth muscle cells.

Semi-quantitative Analyses Areas (μm^2) occupied by each lesion component were evaluated with a VHX Digital Microscope (Keyence Corp., Osaka, Japan). The vulnerability index, an index of the morphological destabilized characteristics of atherosclerotic lesions in WHHLMI rabbits, was calculated for each atherosclerotic lesion as previously described.[23] The vulnerability index was defined as the ratio of the lipid component area (macrophages+extracellular lipid deposits)/fibromuscular component area (smooth muscle cells+collagen fibers). Collagen-rich fibers and extracellular lipid deposits (extracellular vacuoles and lacunae) were determined with Azan–Mallory staining.[19] The macrophage and smooth muscle cell areas were determined with immunohistochemical staining by use of antibodies RAM11 and 1A4, respectively. LOX-1 and TF expression were assessed as percentages of positively stained areas (% positive). The number of TUNEL-positive cell (apoptotic cell) was counted under the microscope and the TUNEL-positive cell density (number/mm^2) was calculated.

In order to evaluate the detailed expression of LOX-1 and TF in atheromatous and fibroatheromatous lesions, these lesions were subdivided into three subregions; fibromuscular cap, lipid area and boundary regions (Fig. 5I).[21] The intensity of immunohistochemical staining for LOX-1 and TF was examined in each subregion and scored from 0 to 2 (0, negative; 1, equivocal; 2, intense). The evaluation was performed in a blinded fashion four times by two independent observers (S.I. and N.T.) for each specimen.

Statistical Analyses Data are presented as the mean± S.D. Comparisons among lesion types were performed using the Kruskal–Wallis test with *post hoc* analysis by the Scheffe test. Correlation coefficients were assessed with Spearman rank correlation coefficients. Statistical significance was defined as $p<0.05$.

RESULTS

Composition of Atherosclerotic Lesions In the aortic arch and thoracic aorta of 4 WHHLMI rabbits, 191 histopathological features which correspond to the classification criteria (neointimal, atheromatous, fibroatheromatous or collagen-rich lesions) were observed. Thus, the 191 regions were divided into the 4 lesion-categories. Figure 1 shows typical images of four categorized lesion types with HE, Azan–Mallory and immunohistochemical staining (Figs. 1A—H). Fourteen lesions were classified as neointimal lesions showing a thin intimal layer consisting of smooth muscle cells and few macrophages (Fig. 1, left column). Forty-four lesions were classified as atheromatous lesions, consisting of a large

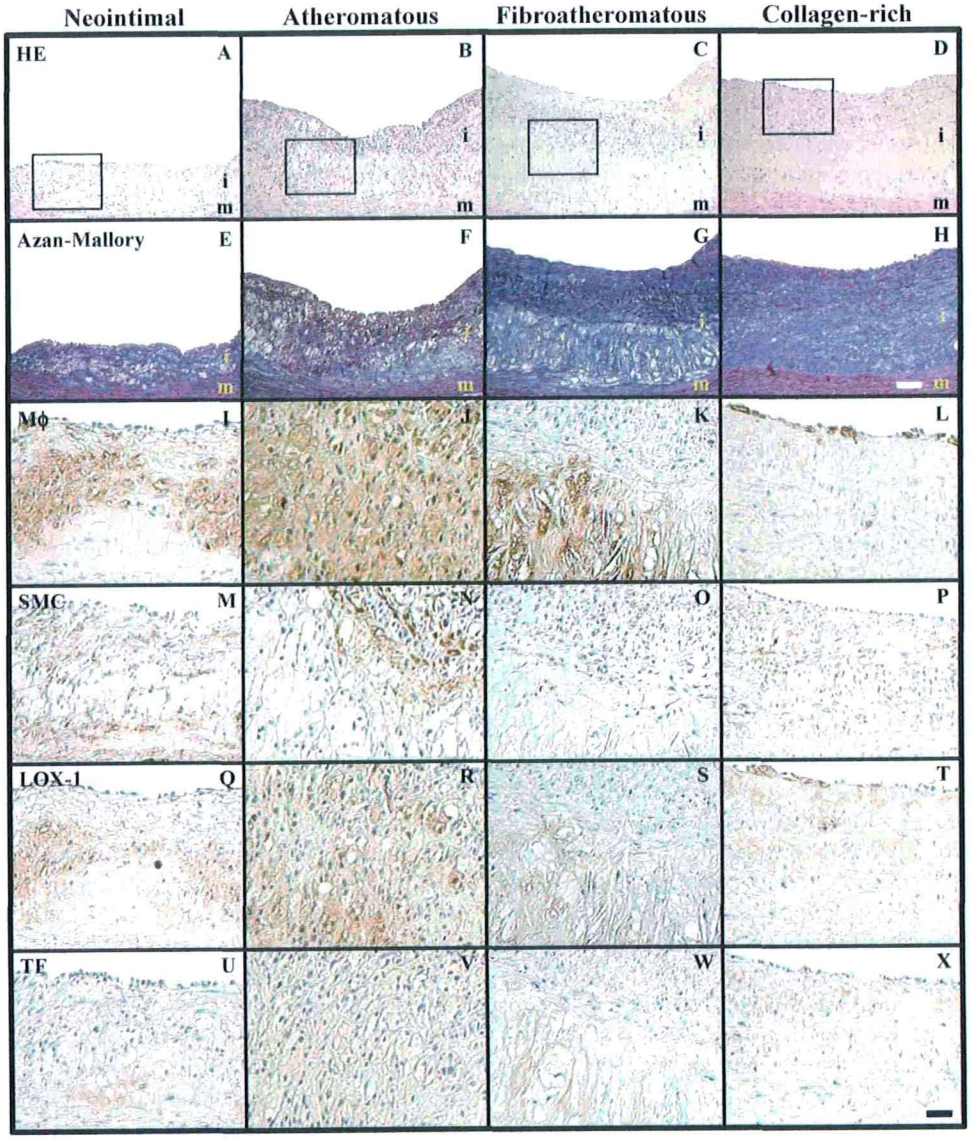

Fig. 1. LOX-1 and TF Expression in 4 Categorized Atherosclerotic Lesions of WHHLMI Rabbits

Atherosclerotic lesions were microscopically classified into four categories as described in Materials and Methods: neointimal lesion (left column), atheromatous lesion (middle-left column), fibroatheromatous lesion (middle-right column) and collagen-rich lesion (right column). HE staining (A—D), Azan–Mallory staining (E—H) and immunohistochemical staining for macrophage staining (Mϕ) (I—L), smooth muscle cell staining (SMC) (M—P), LOX-1 (Q—T) and TF (U—X) are shown. The panels of immunohistochemical staining showed higher magnification images of the area indicated in A—D. Bar=100 μm, magnification ×40 (A—H), Bar=300 μm, magnification ×120 (I—X), m: media, i: intima.

lipid area with abundant macrophages and extracellular lipid deposits, accompanied by a thin fibromuscular cap with relatively few smooth muscle cells scattered in the superficial region (Fig. 1, middle-left column). Fifty-six lesions showed typical characteristics of fibroatheromatous lesions, consisting of few macrophages, less extracellular lipid deposits and a thicker fibromuscular cap (Fig. 1, middle-right column). Seventy-seven lesions were categorized as collagen-rich lesions, consisting of a thick neointimal layer with abundant fibrous connective tissue and smooth muscle cells, while the lipid area was minimal or even absent; collagen-rich lesions (Fig. 1, right column). The atheromatous, fibroatheromatous and collagen-rich lesions were similarly observed in both of the aortic arch and the descending thoracic aorta; however, neointimal lesions were found only in the aortic arch, but not in the descending thoracic aorta. Neither plaque rupture nor thrombi (type VI) were detectable in the aortic arch or the descending thoracic aorta of the rabbits used in the present study.

LOX-1/TF Expression and Apoptotic Events in Atherosclerotic Lesions Prominent LOX-1 expression was found in the macrophage-rich lipid areas of atheromatous and fibroatheromatous lesions (Figs. 1Q—T). LOX-1 expression was also observed in the superficial part of neointimal lesions and collagen-rich lesions. In addition, scattered positive staining for LOX-1 was observed in the neointima of collagen-rich lesions. LOX-1 expression was mainly detected in macrophages and endothelial cells, as well as slight to moderate expression in the smooth muscle cells (Figs. 1I—T). TF expression was prominent in the macrophage-rich lipid areas of atheromatous lesions, and the expression was mainly observed in macrophage foam cells (Figs. 1I—L, U—X). TUNEL-positive cells were extensively observed in the macrophage-rich lipid areas of the atheromatous and fibroatheromatous lesions where a large number of foam cells were accumulated (Figs. 2B, C). Scattered TUNEL-positive

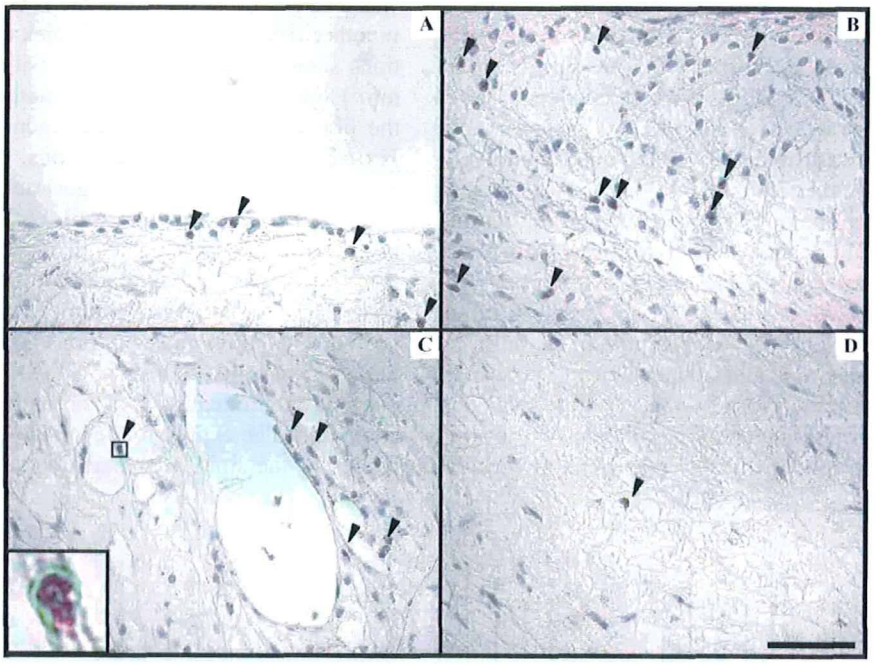

Fig. 2. Detection of TUNEL-Positive Nuclei in 4 Categorized Atherosclerotic Lesions of WHHLMI Rabbits

DNA fragmentation staining by *in situ* end labeling (TUNEL) are shown. Scattered TUNEL-positive nuclei (arrow head) were observed in the intimal region (A), the macrophage-rich lipid area of fibroatheromatous lesion (C) and the collagen layer (D). TUNEL-positive nuclei were mainly observed in the macrophage-rich lipid area of the atheromatous lesion (B). Bar=50 μm, magnification ×300. In panel (C), a higher magnification image of a TUNEL-positive nucleus was indicated (inlet).

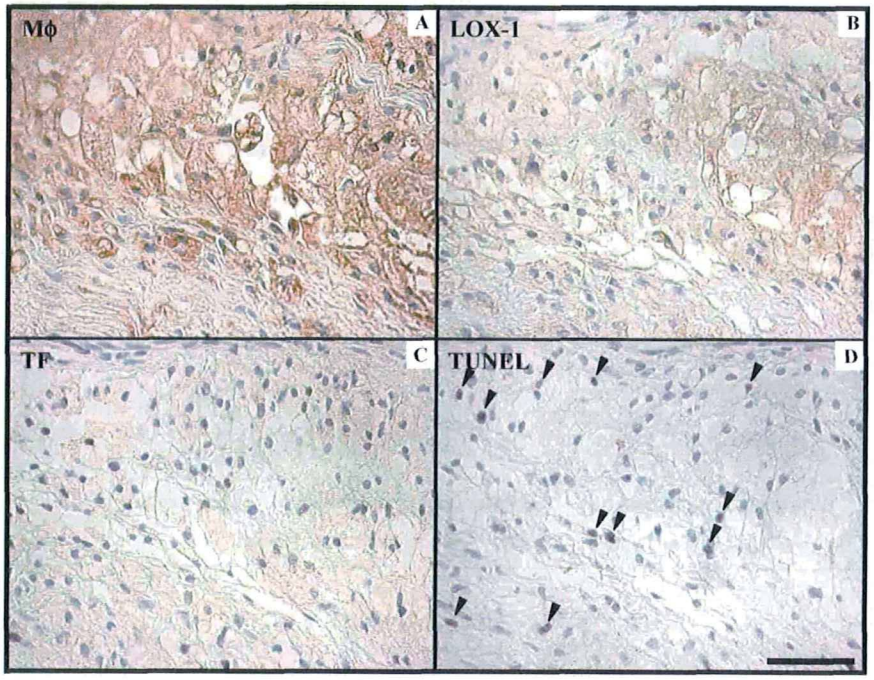

Fig. 3. Typical Microscopic Images of Immunohistochemical Staining for Macrophages (A), LOX-1 (B) and TF (C), and TUNEL Staining (D) for the Macrophage-Rich Area of the Atheromatous Lesion

LOX-1 expression was mainly observed in the macrophage-rich lipid area where TF expression and TUNEL-positive nuclei were prominent. Bar=50 μm, magnifications ×300.

cells were found in the fibromuscular areas of the collagen-rich lesions (Fig. 2D). TUNEL-positive cells in the superficial region were much less frequently seen among all atherosclerotic lesions (Fig. 2A).

Figure 3 shows typical microscopic images of immunostaining and TUNEL for the macrophage-rich lipid area of atheromatous lesions at higher magnifications. LOX-1 expression, TF expression and TUNEL-positive cells were prominently observed in the macrophage-rich lipid areas (Fig. 3).

There was no notable difference in the staining tendency of LOX-1, TF and TUNEL-positive cells between the aortic arch and the descending thoracic aorta. Neither LOX-1, TF, nor TUNEL-positive cells were detectable by immunostain-

ing in negative control sections (data not shown).

Semi-quantitative Analyses of LOX-1/TF Expression and Apoptotic Events in Relation to Plaque Vulnerability Figure 4a shows the vulnerability index calculated for each lesion category classified as described in Materials and Methods. This index was the highest in the atheromatous lesions ($p<0.0001$ *vs.* other lesions), followed in decreasing order by the fibroatheromatous lesions ($p<0.005$ *vs.* neointimal lesions; $p<0.0001$ *vs.* collagen-rich lesions), the neointimal lesions, and the collagen-rich lesions.

LOX-1 expression (% positive) was the highest in the atheromatous lesions ($p<0.05$ *vs.* neointimal lesions; $p<0.0001$ *vs.* fibroatheromatous and collagen-rich lesions, Fig. 4b), followed in decreasing order by the neointimal lesions, the fibroatheromatous lesions, and the collagen-rich lesions. TF expression (% positive) in the atheromatous lesions was also the highest among the four lesion types ($p<0.0001$ *vs.* other lesions, Fig. 4c). DNA nick end-labeling of tissue sections showed that the TUNEL-positive cell density (number/mm^2) was higher in the atheromatous lesions than those in the fibroatheromatous and collagen-rich lesions ($p<0.0001$, Fig. 4d). In the neointimal lesions, the TUNEL-positive cell density was higher than collagen-rich lesions ($p<0.05$).

Localization of LOX-1 and TF Expression within Atherosclerotic Lesions The atheromatous and fibroatheromatous lesions were subdivided into three subregions: fibromuscular cap (C), lipid area (foam cells+extracellular lipid deposits) (L) and boundary regions (B) as illustrated in Fig. 5I. Staining intensity scores for LOX-1 and TF in each subregion of atheromatous and fibroatheromatous lesions were compared. The expression levels of LOX-1 were significantly higher in the lipid area than in the fibromuscular cap and

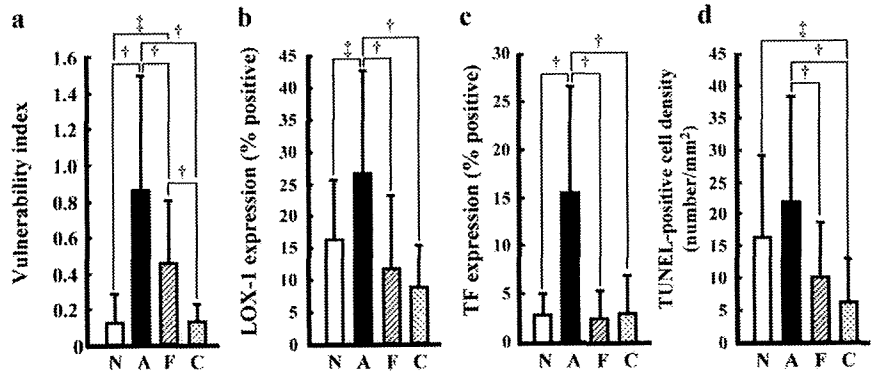

Fig. 4. Vulnerability Index (a), Percentages of Positively Stained Areas (% Positive) for LOX-1 (b) and TF (c), and TUNEL-Positive Cell Density (Number/mm^2) (d) in the Classified Atherosclerotic Lesions

N, A, F and C indicate neointimal, atheromatous, fibroatheromatous and collagen-rich lesions, respectively. Data are represented as the mean±S.D. †$p<0.0001$, ‡$p<0.05$.

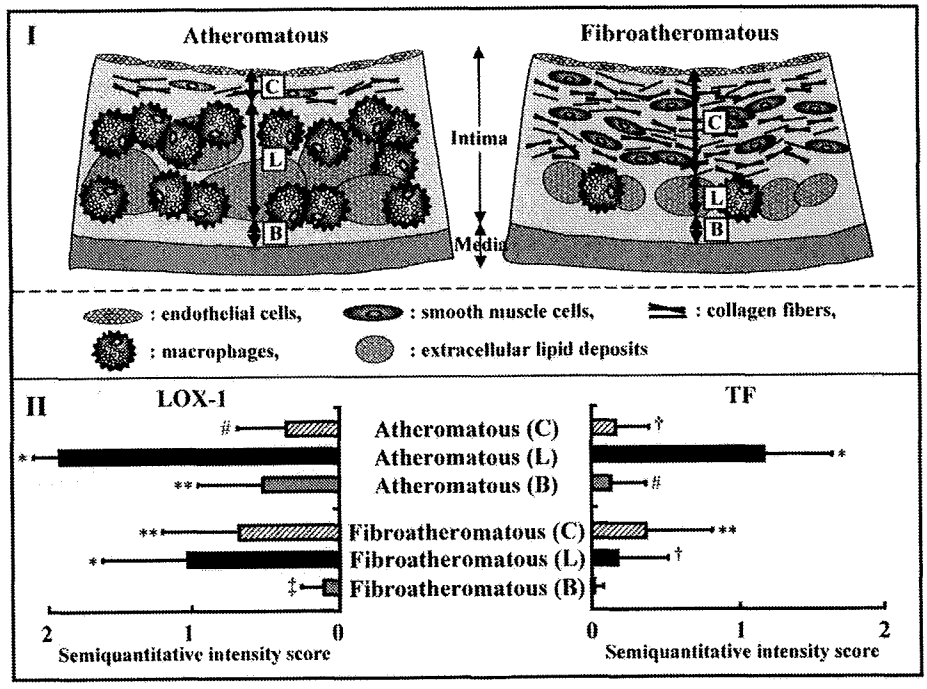

Fig. 5. LOX-1 and TF Expression Scores in Fibromuscular Cap (C), Lipid Area (Foam Cells+Extracellular Lipid) (L), and Boundary (B) Subregions of Atheromatous and Fibroatheromatous Lesions

(I) Schematic illustration of fibromuscular cap (C), lipid area (L) and boundary (B) subregions, which compose atheromatous (left) and fibroatheromatous (right) lesions. (II) Expression scores of LOX-1 (left) and TF (right) in fibromuscular cap (C), lipid area (L) and boundary (B) subregions of 44 atheromatous (upper) and 56 fibroatheromatous (lower) lesions. Data are indicated as the mean±S.D. in each subregion. *$p<0.0001$ *vs.* all other regions. **$p<0.0001$ *vs.* fibroatheromatous (B). #$p<0.0001$ *vs.* fibroatheromatous (C). †$p<0.05$ *vs.* fibroatheromatous (C). ‡$p<0.05$ *vs.* atheromatous (C).

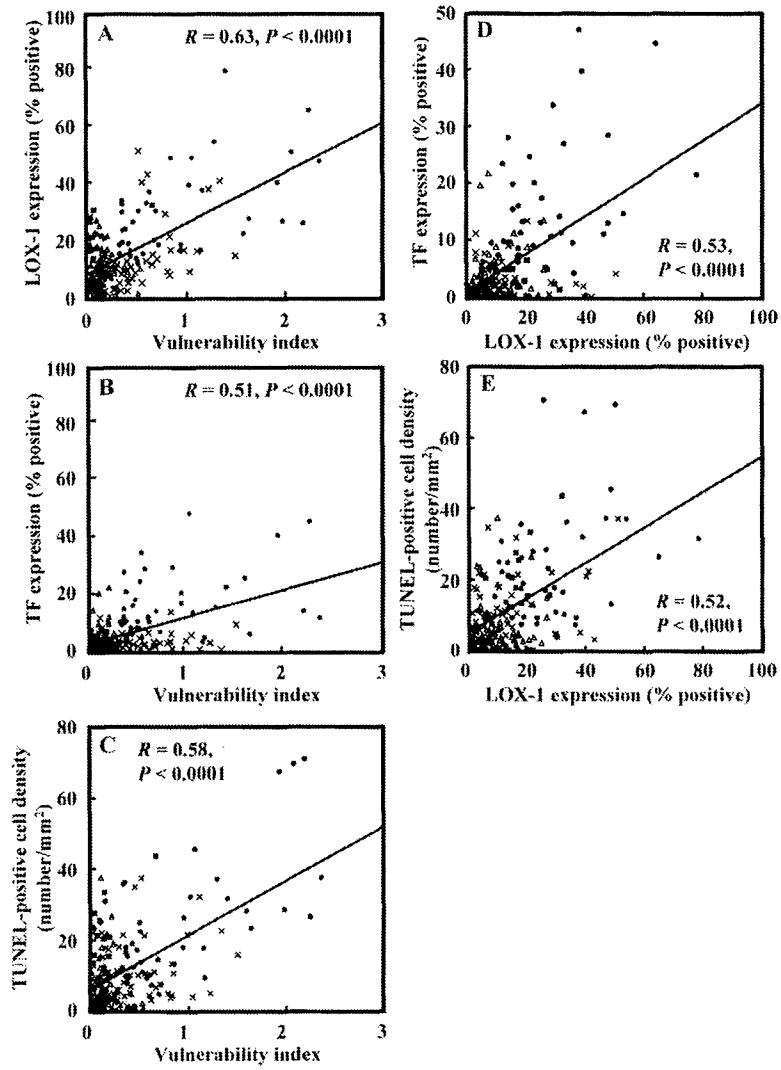

Fig. 6. Analyses of Correlations among LOX-1 and TF Expression (% Positive), and TUNEL-Positive Cell Density (Number/mm^2) and Histological Vulnerability

Regression analyses demonstrated a positive correlation between vulnerability index and LOX-1 expression (r=0.63, p<0.0001) (A), between vulnerability index and TF expression (r=0.51, p<0.0001) (B), as well as between vulnerability index and TUNEL-positive cell density (r=0.58, p<0.0001) (C). In the same manner, a positive correlation between LOX-1 expression and TF expression (r=0.53, p<0.0001), as well as between LOX-1 expression and TUNEL-positive cell density (r=0.52, p<0.0001) are shown in panel (D) and (E), respectively. ■; neointimal, ●; atheromatous, ×; fibroatheromatous, △; collagen-rich lesions.

boundary regions (Fig. 5II). The LOX-1 expression levels were the highest in the lipid area of atheromatous lesions among all subregions of any lesion types (p<0.0001), followed by the lipid area of fibroatheromatous lesions. The TF expression levels were also the highest in the lipid area of atheromatous lesions among all subregions of any lesion types.

Correlation Analyses among LOX-1, TF, Apoptosis and Histological Vulnerability Correlation of the vulnerability index with LOX-1 and TF expression (% positive), and TUNEL-positive cell density (number/mm^2) is shown in Figs. 6A—C. LOX-1 expression was positively correlated with the vulnerability index (r=0.63, p<0.0001, Fig. 6A). Similarly, TF expression and TUNEL-positive cell density showed positive correlation with the vulnerability index (r=0.51, p<0.0001 and r=0.58, p<0.0001, respectively, Figs. 6B, C).

Figures 6D and E show the correlation of LOX-1 expression with TF expression (D) and TUNEL-positive cell density (E). Regression analyses demonstrated positive correlation between LOX-1 and TF expression (r=0.53, p<0.0001, Fig. 6D), as well as between LOX-1 expression and TUNEL-positive cell densities (r=0.52, p<0.0001, Fig. 6E).

DISCUSSION

Our major findings in this study can be summarized as follows: (1) significantly enhanced LOX-1, TF expression and apoptotic events were observed in the atheromatous lesions characteristic of the vulnerable plaque. (2) LOX-1 expression was mainly observed in the macrophage-rich lipid area where TF expression and apoptotic events were prominent. (3) LOX-1 expression levels were positively correlated with morphological vulnerability (vulnerability index), TF expression and apoptotic events. These findings are the first *in vivo* data suggesting the roles of LOX-1 in the processes of plaque destabilization and subsequent thrombus formation.

In the present study, we investigated the LOX-1 expression

in WHHLMI rabbits that developed various atherosclerotic changes, early to advanced lesions, in the same individual. Consequently, we found that the LOX-1 expression was the highest in the atheromatous lesions (type IV) (Fig. 4B), which could mainly be caused by extensive LOX-1 expression in macrophages-rich area (Fig. 1R, 5II left). The current results support our earlier study where we showed a correlation between LOX-1 expression and morphological plaque instability.[16] In addition, Kataoka *et al.* reported LOX-1 expression in macrophages and smooth muscle cells in human advanced atherosclerotic lesions.[24] On the other hand, Chen *et al.* reported that LOX-1 expression was observed in endothelial cells, macrophages and smooth muscle cells in early atherosclerotic lesions.[25] The moderate LOX-1 expression in the neointimal lesions observed in our rabbits was consistent with the results reported by Chen *et al.*

TF has been known as an initiating factor in the coagulation protease cascade. TF expression has been suggested by several studies to be linked with thrombus formation after the plaque rupture. TF expression has been detected within the macrophage-rich areas, but is absent in the fibrous tissue.[26,27] Concordantly, TF expression was extensively shown in the lipid area (Fig. 5II right) of atheromatous lesions (Fig. 4C) in the present study. The spatial distribution of TF and LOX-1 immunostaining in serial sections suggests the colocalization of these antigens in RAM-11-positive macrophage-rich area (Figs. 1, 3A—C, 5). In addition, the TF expression was positively correlated with the LOX-1 expression in the atherosclerotic plaques (Fig. 6D). Thus, our data provide *in vivo* evidence for the correlated expression between LOX-1 and TF. These findings appear to suggest that LOX-1 may be involved in Ox-LDL-induced TF expression in the lipid rich plaques *in vivo*. The CD40/CD40L signaling pathway may be involved in this process, since Ox-LDL-LOX-1 interactions activate the CD40/CD40L signaling pathway,[13,14] which thereby induces TF expression.[15] Thus, LOX-1 may play a key role in TF expression, and thereby thrombus formation *in vivo*. In addition, previous *in vitro* studies have also reported that expression of TF and LOX-1 are mediated by nuclear factor-κB (NF-κB) activation.[28—30] The proinflammatory transcription factor, NF-κB, has been known to mediate transcription of a wide variety of genes induced by proinflammatory simuli, including IL-1α, IL-1β, TNF-α, and Ox-LDL.[31] Therefore, coordinated expression of TF and LOX-1 in the macrophage-rich lipid area of the atheromatous lesions may be regulated by NF-κB.

Apoptosis is one of the causative factors in the formation of vulnerable atherosclerotic plaques. Apoptosis of foam cells and macrophages is thought to promote plaque vulnerability by causing the accumulation of an acellular (cell-poor) lipid core.[4] In the present study, LOX-1 expression was prominent in the macrophage-rich lipid area where TUNEL-positive cells were mainly observed (Figs. 3A—D). When quantified by histomorphometry, the significant correlation between LOX-1 expression and apoptotic events in the atherosclerotic lesions was observed (Fig. 6E). On the other hand, the translocation of phosphatidylserine to the cell surface that occurred during apoptotic cell death was reportedly correlated to a high TF expression.[26,32] Concordantly, we detected marked TF expression in close proximity to apoptotic foam cells within the macrophage-rich lipid area (Figs. 3C, D). Taken together, a potential *in vivo* interaction among LOX-1, TF and apoptotic events may be proposed. LOX-1 may promote TF expression not only *via* the CD40/CD40L signaling pathway, but also the apoptosis of foam cells in the macrophage-rich lipid area of atheromatous lesions. Further studies on the LOX-1-dependent activation of caspase-9 and caspase-3, and/or the regulation of Bcl-2 and c-IAP-1[11] would clarify the potential linkage.

It is also reported that the apoptosis of smooth muscle cells could weaken the fibrous cap *via* a decrease in the synthesis of the extracellular matrix.[5] Previous studies suggested that LOX-1 expression may also play a role in the development of apoptosis in smooth muscle cells.[10,11,24] In the present study, however, TUNEL-positive nuclei were mainly observed in macrophage-rich lipid area where LOX-1 expression is abundant using a rabbit hyperlipidemic model. Several previous studies have indicated that Ox-LDL-LOX-1 interaction in macrophages promotes MMPs involved in the degradation of extracellular matrix proteins,[12] which is consistent with our current and previous results in WHHLMI rabbits.[16]

It is of great importance to discuss the animal model used in the present study (WHHLMI rabbits). Unfortunately, animal models suitable for studying the spontaneous rupture of unstable plaques have yet to be established. However, it has been reported that hemorrhage, plaque rupture and thrombosis (type VI) are occasionally observed in coronary lesions of WHHLMI rabbits, although the atherosclerotic plaques are not prone to rupture.[33] In fact, the pathological features of atheromatous lesions observed in our rabbits were similar to those of human unstable plaques.[17,18,34,35] Thus, the use of WHHLMI rabbits could be effective for investigating causative factors in the destabilization of atherosclerotic plaques and help translate laboratory observations to the clinical setting.

CONCLUSION

The present data from the atherosclerotic specimens of WHHLMI rabbits demonstrate a pathobiological link among LOX-1, TF, apoptotic events and the vulnerability of atherosclerotic plaques, suggesting that the vulnerability and thrombotic activity of atherosclerotic lesions may result from a LOX-1 signal linkage. The present findings should help understand the pathophysiology of atherosclerosis, leading to the development of new therapeutic and diagnostic (imaging) agents of atherosclerosis.

Acknowledgements This work was partly supported by a Grant-in-Aid for General Scientific Research from the Ministry of Education, Culture, Sports, Science and Technology of Japan, and from the Japan Society for the Promotion of Science, by a research grant from New Energy and Industrial Technology Development Organization (NEDO), by a research grant for Cardiovascular diseases from the Ministry of Health, Labor and Welfare (16C-8) and by the 21st Century COE Program, 'Knowledge Information Infrastructure for Genome Science.'

REFERENCES

1) Ruberg F. L., Leopold J. A., Loscalzo J., *Prog. Cardiovasc. Dis.*, **44**, 381—394 (2002).
2) Falk E., Shah P. K., Fuster V., *Circulation*, **92**, 657—671 (1995).
3) Moons A. H., Levi M., Peters R. J., *Cardiovasc. Res.*, **53**, 313—325 (2002).
4) Bjorkerud S., Bjorkerud B., *Am. J. Pathol.*, **149**, 367—380 (1996).
5) Geng Y. J., Henderson L. E., Levesque E. B., Muszynski M., Libby P., *Arterioscler. Thromb. Vasc. Biol.*, **17**, 2200—2208 (1997).
6) Sawamura T., Kume N., Aoyama T., Moriwaki H., Hoshikawa H., Aiba Y., Tanaka T., Miwa S., Katsura Y., Kita T., Masaki T., *Nature* (London), **386**, 73—77 (1997).
7) Li D., Mehta J. L., *Circulation*, **101**, 2889—2895 (2000).
8) Moriwaki H., Kume N., Kataoka H., Murase T., Nishi E., Sawamura T., Masaki T., Kita T., *FEBS Lett.*, **440**, 29—32 (1998).
9) Smirnova I. V., Kajstura M., Sawamura T., Goligorsky M. S., *Am. J. Physiol. Heart Circ. Physiol.*, **287**, 782—790 (2004).
10) Kataoka H., Kume N., Miyamoto S., Minami M., Morimoto M., Hayashida K., Hashimoto N., Kita T., *Arterioscler. Thromb. Vasc. Biol.*, **21**, 955—960 (2001).
11) Kume N., Kita T., *Circ. Res.*, **94**, 269—270 (2004).
12) Li D., Liu L., Chen H., Sawamura T., Ranganathan S., Mehta J. L., *Circulation*, **107**, 612—617 (2003).
13) Li D., Liu L., Chen H., Sawamura T., Mehta J. L., *Arterioscler. Thromb. Vasc. Biol.*, **23**, 816—821 (2003).
14) Schonbeck U., Libby P., *Circ. Res.*, **89**, 1092—1103 (2001).
15) Sanguigni V., Ferro D., Pignatelli P., Del Ben M., Nadia T., Saliola M., Sorge R., Violi F., *J. Am. Coll. Cardiol.*, **45**, 35—42 (2005).
16) Ishino S., Mukai T., Kume N., Asano D., Ogawa M., Kuge Y., Minami M., Kita T., Shiomi M., Saji H., *Atherosclerosis*, **195**, 48—56 (2007).
17) Shiomi M., Ito T., Tsukada T., Yata T., Ueda M., *Arterioscler. Thromb.*, **14**, 931—937 (1994).
18) Shiomi M., Ito T., Yamada S., Kawashima S., Fan J., *Arterioscler. Thromb. Vasc. Biol.*, **23**, 1239—1244 (2003).
19) Ishino S., Kuge Y., Takai N., Tamaki N., Strauss H. W., Blankenberg F. G., Shiomi M., Saji H., *Eur. J. Nucl. Med. Mol. Imaging*, **34**, 889—899 (2007).
20) Stary H. C., Chandler A. B., Glagov S., Guyton J. R., Insull W. Jr., Rosenfeld M. E., Schaffer S. A., Schwartz C. J., Wagner W. D., Wissler R. W., *Circulation*, **89**, 2462—2478 (1994).
21) Stary H. C., Chandler A. B., Dinsmore R. E., Fuster V., Glagov S., Insull W. Jr., Rosenfeld M. E., Schwartz C. J., Wagner W. D., Wissler R. W., *Circulation*, **92**, 1355—1374 (1995).
22) Shiomi M., Ito T., Hirouchi Y., Enomoto M., *Ann. N. Y. Acad. Sci.*, **947**, 419—423 (2001).
23) Shiomi M., Ito T., Hirouchi Y., Enomoto M., *Atherosclerosis*, **157**, 75—84 (2001).
24) Kataoka H., Kume N., Miyamoto S., Minami M., Moriwaki H., Murase T., Sawamura T., Masaki T., Hashimoto N., Kita T., *Circulation*, **99**, 3110—3117 (1999).
25) Chen M., Kakutani M., Minami M., Kataoka H., Kume N., Narumiya S., Kita T., Masaki T., Sawamura T., *Arterioscler. Thromb. Vasc. Biol.*, **20**, 1107—1115 (2000).
26) Hutter R., Valdiviezo C., Sauter B. V., Savontaus M., Chereshnev I., Carrick F. E., Bauriedel G., Lüderitz B., Fallon J. T., Fuster V., Badimon J. J., *Circulation*, **109**, 2001—2008 (2004).
27) Aikawa M., Rabkin E., Sugiyama S., Voglic S. J., Fukumoto Y., Furukawa Y., Shiomi M., Schoen F. J., Libby P., *Circulation*, **103**, 276—283 (2001).
28) Hofnagel O., Luechtenborg B., Eschert H., Weissen-Plenz G., Severs N. J., Robenek H., *Arterioscler. Thromb. Vasc. Biol.*, **26**, 604—610 (2006).
29) Armstead V. E., Opentanova I. L., Minchenko A. G., Lefer A. M., *Anesthesiology*, **91**, 1844—1852 (1999).
30) Parry G. C., Mackman N., *Arterioscler. Thromb. Vasc. Biol.*, **15**, 612—621 (1995).
31) Ghosh S., May M. J., Kopp E. B., *Ann. Rev. Immunol.*, **16**, 225—260 (1998).
32) Mallat Z., Hugel B., Ohan J., Lesèche G., Freyssinet J. M., Tedgui A., *Circulation*, **99**, 348—353 (1999).
33) Shiomi M., Ito T., Yamada S., Kawashima S., Fan J., *J. Atheroscler. Thromb.*, **11**, 184—189 (2004).
34) Kolodgie F. D., Burke A. P., Farb A., Gold H. K., Yuan J., Narula J., Finn A. V., Virmani R., *Curr. Opin. Cardiol.*, **16**, 285—292 (2001).
35) Kullo I. J., Edwards W. D., Schwartz R. S., *Ann. Intern. Med.*, **129**, 1050—1060 (1998).

Targeting of Lectinlike Oxidized Low-Density Lipoprotein Receptor 1 (LOX-1) with ^{99m}Tc-Labeled Anti–LOX-1 Antibody: Potential Agent for Imaging of Vulnerable Plaque

Seigo Ishino[1], Takahiro Mukai[2], Yuji Kuge[1], Noriaki Kume[3], Mikako Ogawa[4], Nozomi Takai[1], Junko Kamihashi[1], Masashi Shiomi[5], Manabu Minami[3], Toru Kita[3], and Hideo Saji[1]

[1]Department of Patho-Functional Bioanalysis, Graduate School of Pharmaceutical Sciences, Kyoto University, Kyoto, Japan; [2]Department of Biomolecular Recognition Chemistry, Graduate School of Pharmaceutical Sciences, Kyushu University, Fukuoka, Japan; [3]Department of Cardiovascular Medicine, Graduate School of Medicine, Kyoto University, Kyoto, Japan; [4]Laboratory of Genome Bio-Photonics Photon Medical Research Center, Hamamatsu University School of Medicine, Hamamatsu, Japan; and [5]Institute for Experimental Animals, Kobe University School of Medicine, Kobe, Japan

Lectinlike oxidized low-density lipoprotein (LDL) receptor 1 (LOX-1), a cell surface receptor for oxidized LDL, has been implicated in vascular cell dysfunction related to plaque instability, which could be a potential target for an atherosclerosis imaging tracer. In this study, we designed and prepared ^{99m}Tc-labeled anti–LOX-1 monoclonal IgG and investigated its usefulness as an atherosclerosis imaging agent. **Methods:** Anti–LOX-1 monoclonal IgG and control mouse IgG2a were labeled with ^{99m}Tc after derivatization with 6-hydrazinonicotinic acid to yield ^{99m}Tc-LOX-1-mAb and ^{99m}Tc-IgG2a, respectively. Myocardial infarction–prone Watanabe heritable hyperlipidemic (WHHLMI) rabbits (atherosclerosis model) and control rabbits were injected intravenously with these probes, and in vivo planar imaging was performed. At 24 h after the injection, the aortas were removed, and radioactivity was measured. Autoradiography and histologic studies were performed with serial aortic sections. **Results:** The level of ^{99m}Tc-LOX-1-mAb accumulation was 2.0-fold higher than the level of ^{99m}Tc-IgG2a accumulation in WHHLMI rabbit aortas, and the level of ^{99m}Tc-LOX-1-mAb accumulation in WHHLMI rabbit aortas was 10.0-fold higher than the level of ^{99m}Tc-LOX-1-mAb accumulation in control rabbit aortas. In vivo imaging clearly visualized the atherosclerotic aortas of WHHLMI rabbits. Autoradiography and histologic studies revealed that regional ^{99m}Tc-IgG2a accumulation was independent of the histologic grade of the lesions; however, regional ^{99m}Tc-LOX-1-mAb accumulation was significantly correlated with LOX-1 expression density and the vulnerability index. The highest level of ^{99m}Tc-LOX-1-mAb accumulation, expressed as {radioactivity in region of interest (Bq/mm^2)/[injected radioactivity (Bq)/animal body weight (g)]} × 10^2, was found in atheromatous lesions (3.8 ± 1.1 [mean ± SD]), followed in decreasing order by fibroatheromatous lesions (2.0 ± 1.0), collagen-rich lesions (1.6 ± 0.8), and neointimal lesions (1.4 ± 0.7). **Conclusion:** The level of ^{99m}Tc-LOX-1-mAb accumulation in grade IV atheroma was higher than that in neointimal lesions or other, more stable lesions. Nuclear imaging of LOX-1 expression with ^{99m}Tc-LOX-1-mAb may be a useful means for predicting atheroma at high risk for rupture.

Key Words: plaque; receptor; antibody; imaging; atherosclerosis
J Nucl Med 2008; 49:1677–1685
DOI: 10.2967/jnumed.107.049536

The spontaneous rupture of vulnerable atherosclerotic plaques and subsequent thrombus formation are currently recognized as the primary mechanisms of myocardial and cerebral infarctions (*1–3*). Evaluation of the vulnerability of atherosclerotic lesions is therefore clinically important for stratifying risk and providing early treatment. At present, however, no noninvasive diagnostic tools for the evaluation of plaque vulnerability are available for routine clinical use. Accordingly, the development of such noninvasive tools is urgently required.

Oxidized low-density lipoprotein (LDL) has been implicated in the pathogenesis of atherosclerosis and atherosclerotic plaque rupture by promoting lipid accumulation and vascular dysfunction. Lectinlike oxidized LDL receptor 1 (LOX-1) mediates the biologic effects of oxidized LDL in this process (*4*). Studies with cultured cells have suggested that LOX-1 may play several important roles in the destabilization of atherosclerotic plaques (*5–9*). Furthermore, our recent animal study indicated that LOX-1 expression in atherosclerotic plaques was positively correlated with plaque instability in vivo (*10*). Accordingly, the detection of LOX-1 expression may help assess the vulnerability of atherosclerotic plaques.

Nuclear medicine imaging enables the visualization of specific molecular processes in vivo and could be used for

Received Dec. 2, 2007; revision accepted Jun. 2, 2008.
For correspondence or reprints contact: Hideo Saji, Department of Patho-Functional Bioanalysis, Graduate School of Pharmaceutical Sciences, Kyoto University, Yoshida Shimoadachi-cho, Sakyo-ku, Kyoto 606-8501, Japan.
E-mail: hsaji@pharm.kyoto-u.ac.jp

imaging of the in vivo biologic properties of atherosclerotic plaques beyond morphologic information (*11,12*). The development of radiopharmaceuticals for the evaluation of plaque vulnerability is a matter of great concern in the clinical diagnosis of atherosclerosis.

In this study, we designed and prepared ^{99m}Tc-labeled anti–LOX-1 monoclonal IgG (^{99m}Tc-LOX-1-mAb) for investigation as an atherosclerosis imaging agent and ^{99m}Tc-labeled control mouse IgG2a (^{99m}Tc-IgG2a) for use as a control probe. Using an atherosclerosis model (myocardial infarction–prone Watanabe heritable hyperlipidemic [WHHLMI] rabbits) (*13*), we compared the accumulation of ^{99m}Tc-LOX-1-mAb and ^{99m}Tc-IgG2a in atherosclerotic lesions with histologic characteristics. Using these data, we evaluated the usefulness of ^{99m}Tc-LOX-1-mAb as an atherosclerosis imaging agent.

MATERIALS AND METHODS

Design and Preparation of ^{99m}Tc-LOX-1-mAb and ^{99m}Tc-IgG2a

A monoclonal antibody for rabbit LOX-1 (mouse IgG2a subtype) was established by use of a standard hybridoma technique (*10,14*). ^{99m}Tc-pertechnetate ($^{99m}TcO_4^-$) from Daiichi Radioisotope Laboratory generators was eluted in saline solution on a daily basis.

Anti–LOX-1 monoclonal IgG (LOX-1-mAb) was radiolabeled with ^{99m}Tc (^{99m}Tc-LOX-1-mAb) after derivatization with 6-hydrazinonicotinic acid (HYNIC) (*15*) according to a previously reported procedure (*16*) with slight modifications. In brief, HYNIC-*N*-hydroxysuccinimide was reacted with LOX-1-mAb, and the mixture was purified by size exclusion chromatography (Sephadex G-50 Fine; Amersham Pharmacia Biotech). To the purified solution of HYNIC–LOX-1-mAb was added an equal volume of ^{99m}Tc-(tricine)$_2$, prepared by the method of Larsen et al. (*17*), to obtain ^{99m}Tc-LOX-1-mAb. After purification of ^{99m}Tc-LOX-1-mAb by centrifugation of a size exclusion column with Sephadex G-50 Fine, the radiochemical purity of ^{99m}Tc-LOX-1-mAb was determined by cellulose acetate electrophoresis (Separax; Joko Co. Ltd.) to be 95.4% ± 2.2% (mean ± SD).

For the control study, negative control mouse IgG2a (Medical & Biologic Laboratories Co. Ltd.) was used for the preparation of ^{99m}Tc-IgG2a [with HYNIC and (tricine)$_2$]. The radiochemical purity of ^{99m}Tc-mouse IgG2a was 97.5% ± 0.9%.

Animal Preparation

All experimental procedures were approved by the Kyoto University Animal Care Committee. Three New Zealand White (NZW) rabbits (male, 3 mo old; Biotec, Inc.) were used to obtain peritoneal macrophages. For ^{99m}Tc-LOX-1-mAb biodistribution studies, 8 WHHLMI rabbits (5 male and 3 female, 11–24 mo old, 3.2 ± 0.5 kg; supplied by the Institute for Experimental Animals, Kobe University School of Medicine) were used. Six NZW rabbits (4 male and 2 female, 3.0 ± 0.3 mo old, 2.6 ± 0.5 kg; Biotec, Inc.) were used for the control study. For ^{99m}Tc-IgG2a biodistribution studies, 3 WHHLMI rabbits (2 male and 1 female, 11–13 mo old, 2.8 ± 0.2 kg) were used. The animals were fed standard chow (type CR-3; Clea Japan Inc.) at 120 g/d and were given water ad libitum.

Immunoreactivity of HYNIC–LOX-1-mAb

Rabbit peritoneal macrophages were obtained by the method of Ishii et al. (*18*) with minor modifications. The cells were suspended in medium A (Dulbecco's modified Eagle's medium containing 1 mM glutamine, penicillin at 100 U/mL, and streptomycin at 100 μg/mL [pH 7.4] as well as 0.2% lactalbumin hydrolysate) at a final concentration of 2.5×10^6 cells/mL. Aliquots of this cell suspension were placed in plastic petri dishes and then cultured in a humidified 5% CO_2 incubator at 37°C. After 2 h, each dish was washed twice with 10 mL of medium A to remove nonadherent cells. The monolayers were cultured for 18 h at 37°C in 20 mL of medium A, and the cells were washed twice with 10 mL of medium A and then used for experiments. More than 95% of the cells were viable, as determined by the trypan blue exclusion test, and almost all of the attached cells showed positive nonspecific esterase staining.

After the macrophages were stimulated for 6 h at 37°C in 5% CO_2 with tumor necrosis factor α at 10 ng/mL (Sigma-Aldrich, Inc.), the cells (10^6) were incubated with LOX-1-mAb (5 μg/mL, 100 μL), HYNIC–LOX-1-mAb (5 μg/mL, 100 μL), or control mouse IgG2a (5 μg/mL, 100 μL) for 30 min at 4°C. This step was followed by washing and incubation with Alexa Fluor 488 goat antimouse IgG (10 μg/mL, 100 μL; Molecular Probes, Inc.) for 30 min at 4°C. For flow cytometry analysis, cells were mixed with Iso-Flow solution (Beckman Coulter Inc.) and immediately analyzed with a FACScan instrument (Becton Dickinson Inc.). Data were analyzed with FACS software (BD CellQuest Pro; BD Biosciences Inc.). The immunoreactivity of HYNIC–LOX-1-mAb was evaluated on the basis of the median fluorescence intensity relative to that of control mouse IgG2a which, in turn, was compared with that of LOX-1-mAb. The measurements were obtained 3 times with rabbit peritoneal macrophages from 3 NZW rabbits, and the ratios were expressed as mean ± SD.

Noninvasive Imaging

After 12 h of fasting, rabbits were initially anesthetized with ketamine (7 mg/kg, intramuscularly) and xylazine (1 mg/kg, intramuscularly). The anesthetic state was maintained with additional doses of ketamine and xylazine during the experimental period. The rabbits were placed on the scanner bed in the prone position to include the abdominal aorta in the field of view. ^{99m}Tc-LOX-1-mAb (1,004 ± 110 MBq, 300 μg) or ^{99m}Tc-IgG2a (733 ± 44 MBq, 300 μg) was injected into a marginal ear vein of the rabbits (3 WHHLMI rabbits and 3 control rabbits for the ^{99m}Tc-LOX-1-mAb study and 3 WHHLMI rabbits for the ^{99m}Tc-IgG2a study). At 10 min and 24 h after injection of the radiotracer, planar images were obtained for 10 min by use of a SPECT-2000H scanner (Hitachi Medical Co.) with a low-energy, high-resolution, parallel-hole collimator having a spatial resolution of 6.7 mm at full width at half maximum. Arterial blood samples were collected from an auricular artery at 24 h. All rabbits were also used in biodistribution studies.

Biodistribution Studies

After rabbits had fasted for 12 h, ^{99m}Tc-LOX-1-mAb (122 ± 65 MBq, 300 μg) or ^{99m}Tc-IgG2a was injected into a marginal ear vein of the rabbits (8 WHHLMI rabbits and 6 control rabbits for the ^{99m}Tc-LOX-1-mAb study and 3 WHHLMI rabbits for the ^{99m}Tc-IgG study). At 24 h after the injection, all of the animals were sacrificed with an overdose of pentobarbital after blood sampling. The ascending aortic arch, the thoracic aorta, the abdominal aorta, the heart, and some femoral muscle were removed. The ascending aortic arch and thoracic and abdominal aortas were cut into 1-cm

segments. Each segment was weighed and immediately fixed in a solution containing L-(+)-lysine hydrochloride (75 mM) and 4% paraformaldehyde in phosphate buffer (37.5 mM, pH 7.4) (*19*). The radioactivity in each sample was measured with a well-type γ-counter (ARC-2000; Aloka). The results were expressed as the differential uptake ratio (DUR), which was calculated as (tissue activity/tissue weight)/(injected radiotracer activity/animal body weight), with activities given in becquerels and weights given in grams. The aorta-to-blood ratio (A/B ratio) and the aorta-to-muscle ratio (A/M ratio) were calculated from the DUR for each tissue sample.

Autoradiography (ARG) Studies

A total of 8 segments, the second and fifth segments of the ascending aortic arch and the second, fifth, and eighth segments each of the thoracic and abdominal aortas, from each animal were used for ARG studies. These segments were frozen and cut into 20-μm-thick slices with a cryomicrotome. The sections were thawed and mounted on silane-coated slides, which were then placed on a phosphorimaging plate (Fuji Imaging Plate BAS-UR; Fuji Photo Film) for 24 h together with a calibrated standard ($^{99m}TcO_4^-$ solution) to obtain ^{99m}Tc-LOX-1-mAb autoradiograms. The ARG images were analyzed by use of a computerized imaging analysis system (Bio Imaging Analyzer BAS3000 and Image Gauge Software; Fuji Photo Film). The radioactivity in each region of interest (ROI) was expressed as {radioactivity in ROI (Bq/mm^2)/[injected radioactivity (Bq)/animal body weight (g)]} × 10^2.

Histologic Analysis

The tissue sections used for ARG studies were also subjected to Azan–Mallory staining and hematoxylin–eosin (HE) staining. Therefore, ARG images were coincident with Azan–Mallory and HE images. Serial sections of the slices from the ARG studies were subjected to immunohistochemical staining (for LOX-1, macrophages, and smooth muscle cells). LOX-1 immunohistochemical staining was performed with LOX-1-mAb and an Envision+ kit (Dako) with hematoxylin counterstaining. In the same manner, immunohistochemical staining for macrophages and smooth muscle cells was performed with rabbit macrophage–specific monoclonal antibody RAM-11 (Dako) and human smooth muscle actin–specific monoclonal antibody 1A4 (Dako), respectively. Immunostaining with subclass-matched irrelevant IgG served as a negative control. Azan–Mallory staining and HE staining were performed by standard procedures. LOX-1 expression density was determined as a percentage of the positively stained region by use of a VHX digital microscope (Keyence Corp.).

To evaluate the correlation of ^{99m}Tc-LOX-1-mAb accumulation with LOX-1 expression density (Fig. 1), we divided each ARG image into 4 ROIs with vertical and horizontal lines as depicted in Figure 2B (dotted line) and then transferred the ROIs to the corresponding immunohistologic image (Fig. 2D, dotted line).

Definition of Atherosclerotic Lesions

Atherosclerotic lesions in WHHLMI rabbit aortas were divided into 4 categories by use of a classification scheme based on the recommendations of the American Heart Association (AHA) (*20,21*) and involving Azan–Mallory staining and HE staining as previously described (*22*): neointimal lesions (types I–III), atheromatous lesions (type IV), fibroatheromatous lesions (types Va and Vb), and collagen-rich lesions (type Vc) (Figs. 3 and 4).

Neointimal lesions (n = 28 for ^{99m}Tc-LOX-1-mAb study and n = 7 for ^{99m}Tc-IgG2a study) were defined as having adaptive thickening of the intima consisting of mainly smooth muscle cells and few macrophages. Atheromatous lesions (n = 46 and n = 20, respectively) contained thin fibrous connective tissue and a dense accumulation of extracellular lipid and foam cells and might correspond to apparently vulnerable lesions in human atherosclerotic plaques.

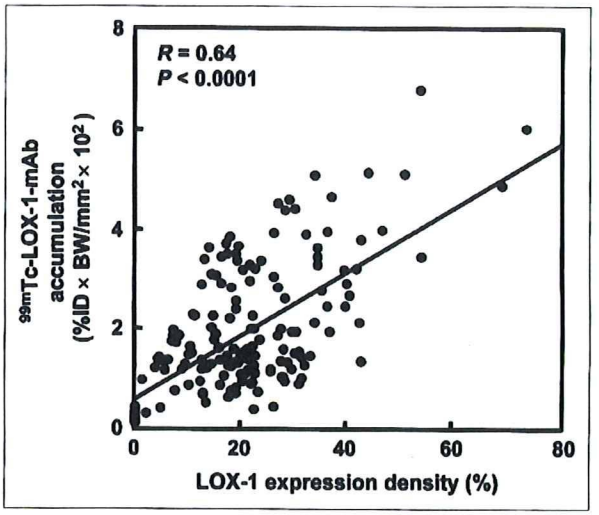

FIGURE 1. Correlation between ^{99m}Tc-LOX-1-mAb accumulation and LOX-1 expression density. Quantitative analysis of autoradiograms provided ^{99m}Tc-LOX-1-mAb accumulation, expressed as {radioactivity in ROI (Bq/mm^2)/[injected radioactivity (Bq)/animal body weight (g)]} × 10^2 (%ID × BW/mm^2 × 10^2).

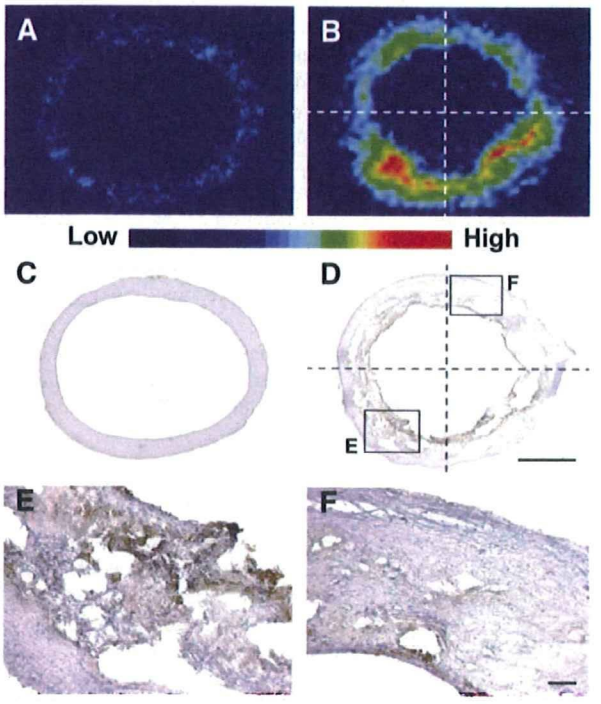

FIGURE 2. Regional distribution of ^{99m}Tc-LOX-1-mAb and LOX-1 expression in aortic sections. (A–D) Autoradiograms (A and B) and LOX-1 immunohistochemical staining (C and D) of control (A and C) and WHHLMI (B and D) rabbits. (E and F) High-magnification images of LOX-1 immunohistochemical staining from insets in D. Bars = 1 mm (C and D) and 100 μm (E and F).

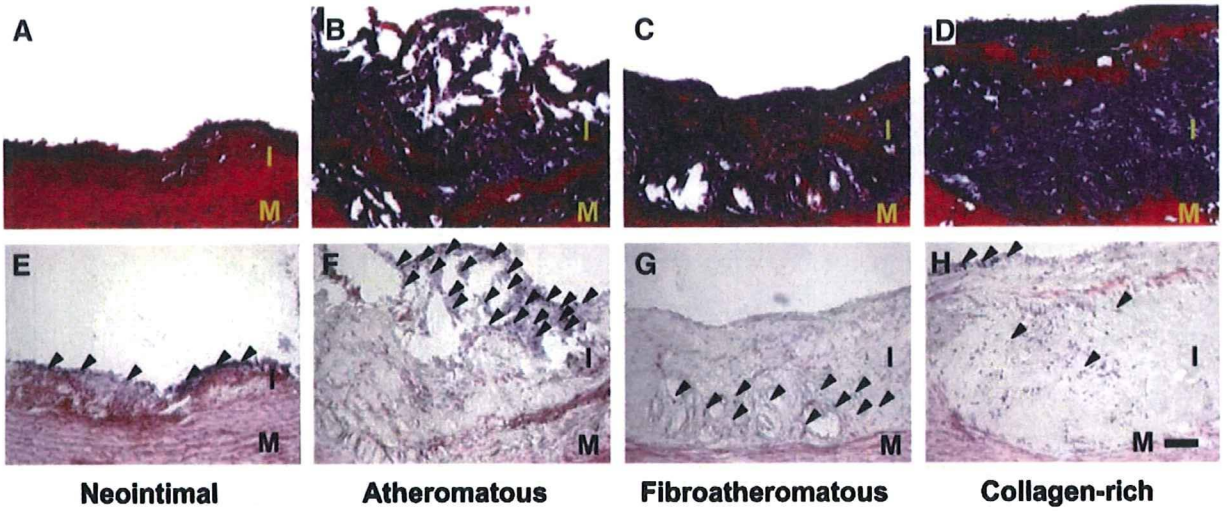

FIGURE 3. Representative photomicrographs of lesion types assigned with AHA classification scheme. (A–D) Azan–Mallory staining. (E–H) HE staining. Arrowheads mark inflammatory cell nuclei. I = intima; M = media. Bar = 100 μm.

Fibroatheromatous lesions (n = 45 and n = 17, respectively) were composed of several lipid cores separated by thick layers of fibromuscular connective tissue and might be stable against rupture (*23–25*). Collagen-rich lesions (n = 73 and n = 49, respectively) consisted of a predominantly collagenous component and contained smooth muscle cells. No lesions showed hemorrhage, plaque rupture, or thrombosis (type VI).

ROIs were placed over the atherosclerotic lesions in the WHHLMI rabbit aortic sections with reference to the classification scheme based on the Azan–Mallory and HE staining images and then were transferred to the corresponding ARG images.

Vulnerability Index

An index of morphologic destabilization characteristics, the vulnerability index, was calculated for each lesion in the WHHLMI rabbits by the method of Shiomi et al. (*26*) The vulnerability index was defined as the ratio of the lipid component area (macrophages and extracellular lipid deposits) to the fibromuscular component area (smooth muscle cells and collagen fibers). Collagen fibers and extracellular lipid deposits (extracellular vacuoles and lacunae) were determined with Azan–Mallory staining. Macrophages and smooth muscle cells were determined with immunohistochemical staining (RAM-11 and 1A4).

Statistical Analysis

Data are presented as mean ± SD. Statistical analysis was performed by use of the Mann–Whitney U test to compare aortic segments in WHHLMI and control rabbits (Table 1). Correlation coefficients were assessed by use of Spearman rank analysis (Figs. 1 and 5). Comparisons among lesion types were performed by use of the Kruskal–Wallis test, and post hoc analysis was performed by use of the Scheffe test (Fig. 6). A P value (2-tailed) of less than 0.05 was considered statistically significant.

RESULTS

Immunoreactivity of HYNIC–LOX-1-mAb

The median fluorescence intensity ratios for LOX-1-mAb and HYNIC–LOX-1-mAb relative to control mouse IgG2a were 1.63 ± 0.08 and 1.52 ± 0.11, respectively, indicating that the immunoreactivity of HYNIC–LOX-1-mAb was 93% that of LOX-1-mAb.

Noninvasive Imaging

The planar images showed primarily blood-pool radioactivity in the abdominal aorta at 10 min after the injection of ^{99m}Tc-LOX-1-mAb or ^{99m}Tc-IgG2a into WHHLMI and control rabbits (Figs. 7A–7C). At 24 h, with decreased blood-pool radioactivity in the abdominal aorta, the atherosclerotic abdominal aorta with ^{99m}Tc-LOX-1-mAb was more clearly visible than the control aorta with ^{99m}Tc-LOX-1-mAb or the atherosclerotic aorta with ^{99m}Tc-IgG2a (Figs. 7D–7F).

Biodistribution Studies

The distributions of ^{99m}Tc-LOX-1-mAb and ^{99m}Tc-IgG2a in the aortic segments of WHHLMI and control rabbits are summarized in Table 1. The level of ^{99m}Tc-LOX-1-mAb accumulation in each aortic segment in WHHLMI rabbits was 7.9- to 12.1-fold higher than that in control rabbits, and the differences were significant. A significant difference in ^{99m}Tc-LOX-1-mAb accumulation was not observed between young WHHLMI rabbits (11–13 mo) and old WHHLMI rabbits (20–24 mo) (DURs of 3.3 ± 1.4 and 2.8 ± 2.1, respectively). Blood-pool radioactivity levels (DURs) at 24 h were 4.5 ± 0.5 and 3.5 ± 0.4 in WHHLMI and control rabbits, respectively. A/B and A/M ratios were significantly higher in WHHLMI rabbits than in control rabbits. Relatively high levels of ^{99m}Tc-LOX-1-mAb accumulation were found in the liver, spleen, and kidneys in both groups of rabbits (data not shown). No marked difference in the distribution of ^{99m}Tc-LOX-1-mAb in nontarget organs was observed between WHHLMI and control rabbits.

The level of ^{99m}Tc-LOX-1-mAb accumulation in WHHLMI rabbit aortas was 1.8- to 2.5-fold higher than the level of ^{99m}Tc-IgG2a accumulation, and the differences were significant.

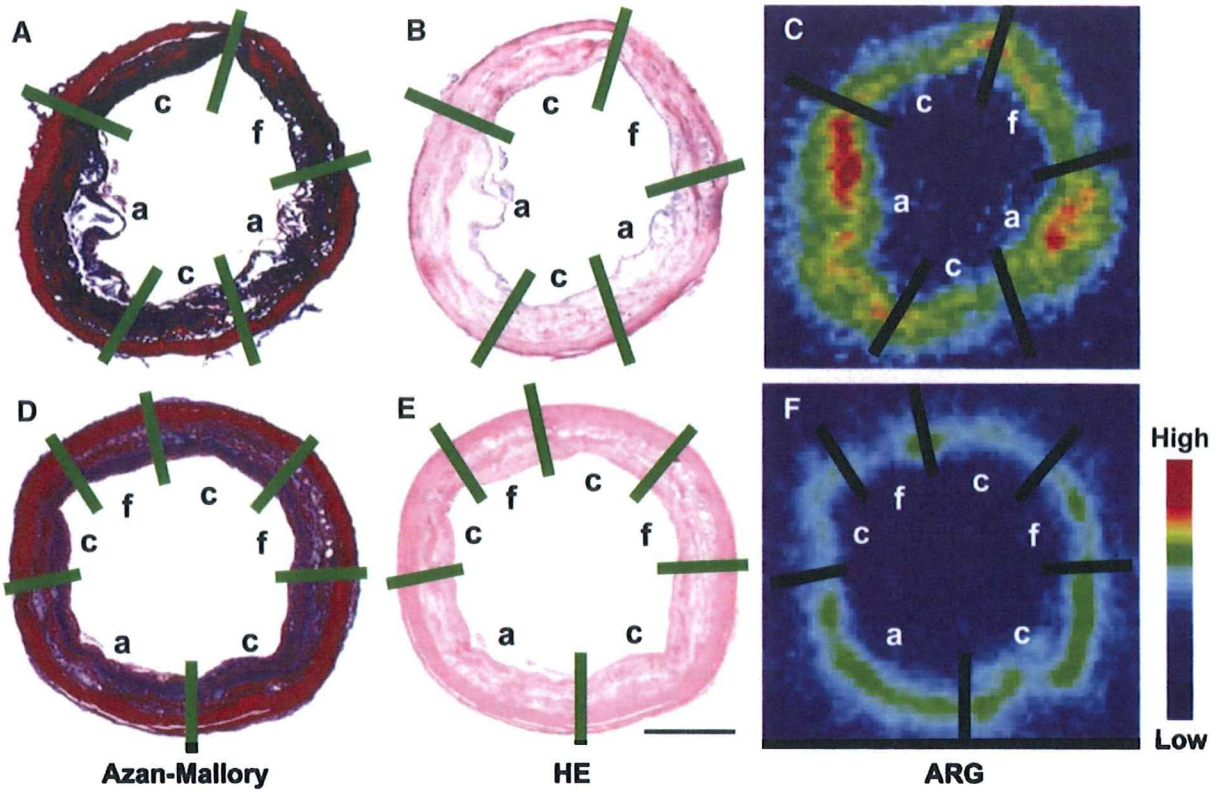

FIGURE 4. Lesion classification scheme in representative photomicrographs and autoradiograms of cross sections of WHHLMI rabbit aortas in ^{99m}Tc-LOX-1-mAb study (A–C) and ^{99m}Tc-IgG2a study (D–F). Atherosclerotic lesions were assigned with AHA classification scheme from Azan–Mallory staining (A and D) and HE staining (B and E) (Fig. 3). Same classification was applied to autoradiograms (ARG) (C and F). ROIs were placed over atherosclerotic lesions in WHHLMI rabbit aortic sections by reference to images with classification scheme from Azan–Mallory staining. a = atheromatous lesions; c = collagen-rich lesions; f = fibroatheromatous lesions. Bar = 1 mm.

Correlation of Regional Distribution of ^{99m}Tc-LOX-1-mAb with LOX-1 Expression

In the ARG studies, heterogeneous ^{99m}Tc-LOX-1-mAb accumulation was observed in the intima of the WHHLMI rabbit aortas, whereas there was little accumulation in the aortas of control rabbits (Figs. 2A and 2B). LOX-1 expression was detected in intimal lesions in WHHLMI rabbit aortas, and the levels of expression differed among the regions (Fig. 2D). As shown in Figures 2B and 2D, higher levels of accumulation of ^{99m}Tc-LOX-1-mAb were observed in regions with high levels of LOX-1 expression, whereas lower levels of accumulation were seen in regions with low levels of LOX-1 expression. Consequently, regional ^{99m}Tc-LOX-1-mAb accumulation in WHHLMI rabbit aortic sections was significantly correlated with LOX-1 expression density (r = 0.64, $P < 0.0001$) (Fig. 1). No obvious LOX-1 expression was observed in the aortas of control rabbits (Fig. 2C).

Correlation of Accumulation of ^{99m}Tc-LOX-1-mAb and ^{99m}Tc-IgG2a with Histologic Characteristics

^{99m}Tc-LOX-1-mAb accumulation was dependent on the histologic grade of lesions (Figs. 4C and 6A), and the highest (and significant; $P < 0.0001$) level was seen in atheromatous lesions (type IV), followed in decreasing order by fibroatheromatous, collagen-rich, and neointimal lesions. Figures 6B and 6C show the macrophage density and vulnerability index quantified for each lesion in the ^{99m}Tc-LOX-1-mAb study. The macrophage density and vulnerability index were also the highest in atheromatous lesions, followed in decreasing order by fibroatheromatous, neointimal, and collagen-rich lesions. Consequently, the highest values for ^{99m}Tc-LOX-1-mAb accumulation, macrophage density, and the vulnerability index were observed in atheromatous lesions. In contrast, lower values for ^{99m}Tc-LOX-1-mAb accumulation, macrophage density, and the vulnerability index were seen in collagen-rich and neointimal lesions. Figure 5A shows the regression analysis for ^{99m}Tc-LOX-1-mAb accumulation and the vulnerability index. The regression analysis demonstrated a directly proportional relationship between ^{99m}Tc-LOX-1-mAb accumulation and the vulnerability index (r = 0.67, $P < 0.0001$).

In contrast, control tracer (^{99m}Tc-IgG2a) accumulation was independent of the histologic grade of lesions, and the differences among the lesions were not significant (Figs. 4F

TABLE 1
Distributions of ^{99m}Tc-LOX-1-mAb and ^{99m}Tc-IgG2a in Aortic Segments of Control and WHHLMI Rabbits at 24 Hours After Injection

Parameter	Mean ± SD for: ^{99m}Tc-LOX-1-mAb in: Control rabbits	^{99m}Tc-LOX-1-mAb in: WHHLMI rabbits	^{99m}Tc-IgG2a in WHHLMI rabbits
Aortic segment*			
Arch (ascending)	0.45 ± 0.19†	4.0 ± 2.0†	1.6 ± 0.4†
Thoracic	0.29 ± 0.17†	3.5 ± 1.1‡	1.9 ± 0.3†§
Abdominal	0.29 ± 0.15†	2.3 ± 1.2	1.3 ± 0.6‖
Total	0.32 ± 0.17†	3.2 ± 1.6	1.6 ± 0.5†
A/B ratio	0.12 ± 0.08†	0.69 ± 0.33	0.33 ± 0.11†
A/M ratio	3.1 ± 1.4†	30.8 ± 16.5	18.1 ± 9.8†

*Reported as DUR.
†$P < 0.0001$ vs. WHHLMI rabbits in ^{99m}Tc-LOX-1-mAb study.
‡$P < 0.0001$ vs. abdominal aorta.
§$P < 0.001$ vs. abdominal aorta.
‖$P < 0.05$ vs. WHHLMI rabbits in ^{99m}Tc-LOX-1-mAb study.
Accumulation in each aortic segment was significantly higher in WHHLMI rabbits than in control rabbits. Ascending arch of aorta and thoracic aorta showed higher radioactivity than abdominal aorta in WHHLMI rabbits.

and 6C). The ^{99m}Tc-IgG2a distribution based on the lesion classification was different from that of ^{99m}Tc-LOX-1-mAb, although the distributions of macrophage density and the vulnerability index in the ^{99m}Tc-IgG2a study were similar to those in the ^{99m}Tc-LOX-1-mAb study (data not shown). Furthermore, no correlation between ^{99m}Tc-IgG2a accumulation and the vulnerability index was shown ($r = 0.002$, $P < 0.0001$) (Fig. 5B).

DISCUSSION

There is an urgent need to develop a means to discriminate vulnerable atherosclerotic lesions (atheromatous lesions) from potentially stable lesions in clinical practice, because the disruption of vulnerable plaques causes myocardial and cerebral infarctions. In the present study, we designed and prepared a new imaging agent, ^{99m}Tc-LOX-1-mAb. Our results clearly indicated the potential of ^{99m}Tc-LOX-1-mAb for targeting LOX-1 and evaluating the vulnerability of atherosclerotic lesions.

The immunoreactivity of an agent is an essential factor in in vivo imaging with immunodetection. Flow cytometry analyses indicated that the modification of LOX-1-mAb with the chelating moiety (HYNIC) did not significantly affect the immunoreactivity of the original LOX-1-mAb, although the mean fluorescence intensity was low. Furthermore, ARG and immunohistochemical studies showed that ^{99m}Tc-LOX-1-mAb accumulation in atherosclerotic lesions was well correlated with LOX-1 expression density (Fig. 1). These results suggested the potential of ^{99m}Tc-LOX-1-mAb to specifically recognize LOX-1 in vivo.

The highest level of ^{99m}Tc-LOX-1-mAb accumulation was seen in atheromatous lesions (Fig. 6A) and was significantly correlated with the vulnerability index (Fig. 5A), indicating the ability of this agent to distinguish apparently vulnerable atheromatous lesions from more stable, chronic plaques. This result is consistent with the in vivo relationship between LOX-1 expression and lesion vulnerability (*10*). In contrast, the relationship between ^{99m}Tc-LOX-1-mAb accu-

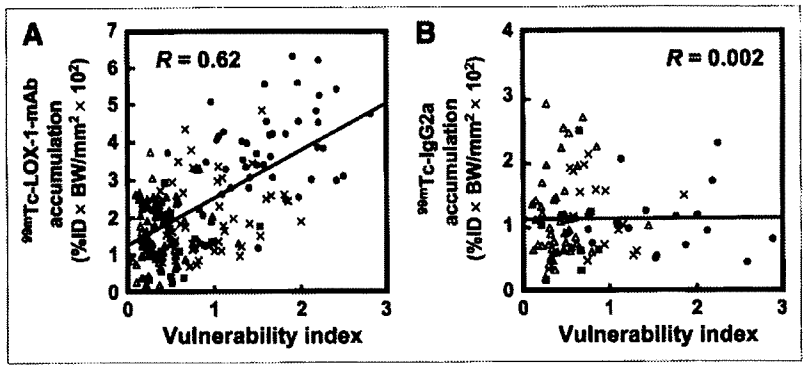

FIGURE 5. Simple regression analyses of vulnerability index with ^{99m}Tc-LOX-1-mAb accumulation (A) and ^{99m}Tc-IgG2a accumulation (B). See legend to Fig. 1 for explanation of units. ● = atheromatous lesion; △ = collagen-rich lesion; × = fibroatheromatous lesion; ■ = neointimal lesion.

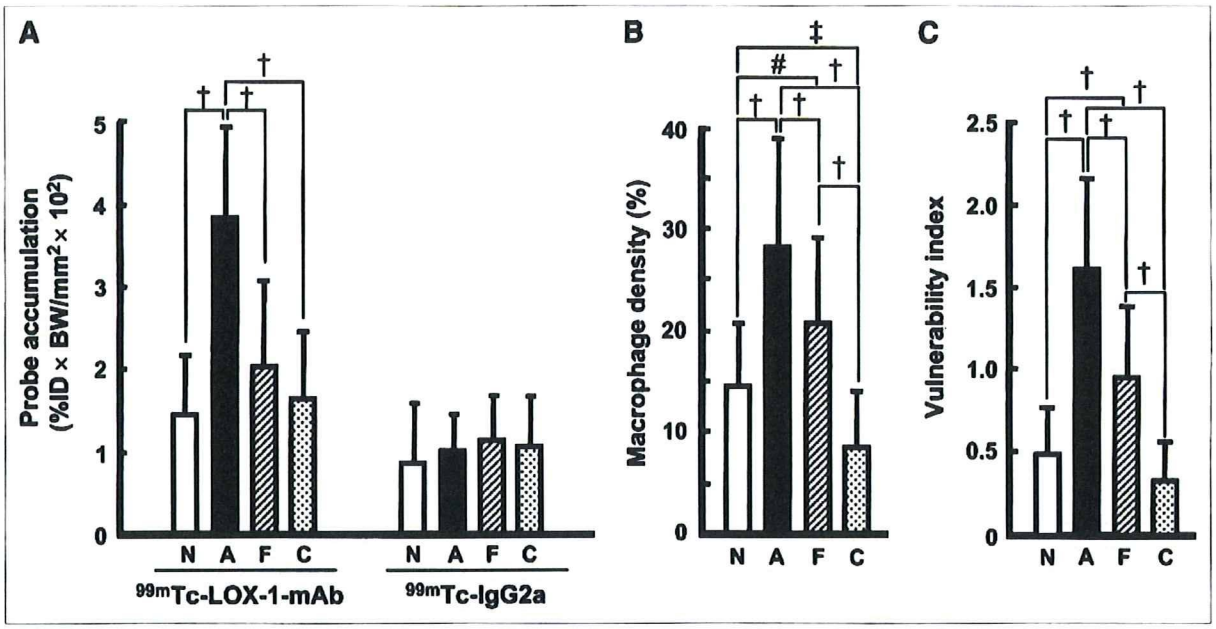

FIGURE 6. Distributions of ^{99m}Tc-LOX-1-mAb and ^{99m}Tc-IgG2a (A) and macrophage density (B) and vulnerability index (C) for each lesion type in ^{99m}Tc-LOX-1-mAb study. Quantitative analysis of autoradiograms provided ^{99m}Tc-LOX-1-mAb and ^{99m}Tc-IgG2a accumulation, expressed as %ID × BW/mm² × 10² (see legend to Fig. 1 for explanation of units). Data are presented as mean ± SD. †$P < 0.0001$. ‡$P < 0.01$. #$P < 0.05$. A = atheromatous lesions; C = collagen-rich lesions; F = fibroatheromatous lesions; N = neointimal lesions.

mulation (LOX-1 signal) and macrophage density was not high ($r = 0.49$, $P < 0.001$) (data not shown), compared with the relationship with the vulnerability index (Fig. 5A). It has been reported that LOX-1 is intensely expressed in endothelial cells and macrophages (foam cells) in unstable atherosclerotic plaques (*10,27*). In the present study, LOX-1 expression was mainly observed in macrophages; however, LOX-1 was also expressed in endothelial cells and smooth muscle cells. LOX-1 plays multiphasic roles in the formation of vulnerable atherosclerotic plaques (*5–9*). Accordingly, although ^{99m}Tc-LOX-1-mAb accumulation is not highly correlated with macrophage density, ^{99m}Tc-LOX-1-mAb should provide clinically useful information about atherogenesis on the basis of the LOX-1 expression level.

In the present study, we applied a nuclear imaging technique for atherosclerosis imaging. Nuclear imaging is used with the aim of visualizing the biologic properties of atherosclerotic plaques (e.g., cellular composition, inflammatory

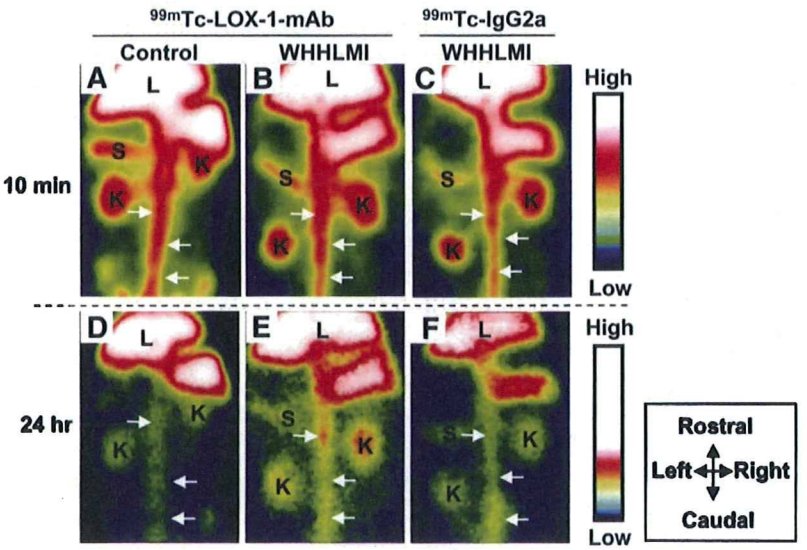

FIGURE 7. Noninvasive imaging of abdominal region with ^{99m}Tc-LOX-1-mAb (A, B, D, and E) and ^{99m}Tc-IgG2a (C and F). Planar images for WHHLMI (B, C, E, and F) and control (A and D) rabbits at 10 min (A–C) and 24 h (D–F) after injection are shown. Field of view = 170 × 120 mm. Arrows = aorta; K = kidney; L = liver; S = spleen.